1 **Dating protracted fault activities: microstructures, microchemistry and geochronology of the**

2 **Vaikrita Thrust, Main Central Thrust zone, Garhwal Himalaya, NW India**

3

4 Chiara Montemagni[1*], Chiara Montomoli[2], Salvatore Iaccarino[3], Rodolfo Carosi[3], Arvind K. Jain[4],

5 Hans-J. Massonne[5] & Igor M. Villa[1,6,7]

6

7 1 - Dipartimento di Scienze dell'Ambiente e della Terra, Università degli Studi di Milano Bicocca,

8 Piazza della Scienza 4, 20126 Milano, Italy

9 2 - Dipartimento di Scienze della Terra, Università di Pisa, v. S. Maria 53, 56126 Pisa, Italy

10 3 - Dipartimento di Scienze della Terra, Università di Torino, v. Valperga Caluso 35, 10125,

11 Torino, Italy

12 4 - CSIR-Central Building Research Institute, Roorkee -247667, Uttarakhand, India

13 5 - Institut für Mineralogie und Kristallchemie, Universität Stuttgart, Azenbergstraße 18, D-70049

14 Stuttgart, Germany

15 6 - Institut für Geologie, Universität Bern, Baltzerstrasse 3, 3012 Bern, Switzerland

16 7 - Centro Universitario Datazioni e Archeometria, Università degli Studi di Milano Bicocca, 20126

17 Milano, Italy

18

19 *Corresponding author (c.montemagni@campus.unimib.it)

20

21 **Short Title**

22 Geochronology of the Vaikrita Thrust

23

24 **Abstract**

25 The timing of shearing along the Vaikrita Thrust, the structurally upper boundary of the Main

26 Central Thrust zone (MCTz), was constrained by combined microstructural, microchemical and

27 geochronological investigations. Three different biotite-muscovite growth and recrystallisation

28 episodes were observed: a relict mica-1; mica-2 along the main mylonitic foliation; mica-3 in

29 coronitic structures around garnet during its breakdown.

30 Analyses of biotite by electron microprobe show chloritization, and bimodal composition of biotite-

31 2 in one sample. Muscovite-2 and muscovite-3 differ in composition from each other.

32 Biotite and muscovite ^{39}Ar-^{40}Ar age spectra from all samples give both inter-sample and intra-

33 sample discrepancies. Biotite step ages range between 8.6 and 16 Ma, muscovite step ages between

34 3.6 and 7.8 Ma. These ages cannot be interpreted as "cooling ages", as samples from the same

35 outcrop cooled simultaneously. Instead, Ar systematics reflect sample-specific

36 recrystallisation markers. Intergrown impurities were diagnosed by Ca/K ratios. Age data of biotite

37 were interpreted as a mixture of true biotite-2 (9.00±0.10 Ma) and two alteration products. The

38 negative Cl/K-age correlation identifies a Cl-poor muscovite-2 (>7 Ma) and a Cl-rich, post-

39 deformational, coronitic muscovite-3 grown at ≤5.88±0.03 Ma. The Vaikrita Thrust was active at

40 least from 9 to 6 Ma around 600 °C; its movement ceased by 6 Ma. Constraining the age and

41 duration of movements in shear zones is one of the major objectives in the study of the evolution of

42 collisional belts (Challandes *et al.* 2003; Di Vincenzo *et al.* 2004; Carosi *et al.* 2006, 2010, 2016;

43 Iaccarino *et al*., 2015, 2017a; Beltrando *et al.* 2009; Rolland *et al.* 2009; Sanchez *et al.* 2011;

44 Montomoli *et al.* 2013, 2015; Cottle *et al.* 2015, Kellett *et al.* 2016), such as the Himalaya (Fig. 1a).

45 One of the main unsolved problems in the Himalayan belt is the nature of the Main Central Thrust

46 (MCT), a first-order tectonic discontinuity that runs all over the length of the belt. The MCT, which

47 divides the Greater Himalayan Sequence (GHS) from the underlying Lesser Himalayan Sequence

48 (LHS), is a top to the S/SW ductile to brittle shear zone, dipping to the north. As discussed by

49 Searle *et al.* (2008), Martin (2016) and Mukhopadhyay *et al.* (2017), the definition of the MCT has

50 changed since the first one by Heim & Gansser (1939). The current debate is especially related to

51 the criteria to define (and, thus, to localise) the MCT. Therefore, several definitions of the MCT

52 have been proposed (see Searle *et al.* 2008, and Martin 2016 for an updated review) such as (1) a

53 structural-metamorphic one (Heim & Gansser 1939); (2) a metamorphic-rheological (Searle *et al.*

54 2008) and a purely rheological one (e.g. Gibson *et al.* 2016; Parsons *et al.* 2016); (3) a

55 chronological one (e.g. Webb *et al.* 2013); and (4) a compositional one, assuming that the MCT is a

56 high-strain reverse kinematic zone that separates distinguishable protoliths (e.g. Martin *et al.* 2005;

57 Martin 2016). Moreover, the MCT records a protracted deformation, from ductile to brittle (Carosi

58 *et al.* 2007, and references therein), and affects several different lithologies along strike. This

59 further complicates the debate.

60 The above controversy led to the definition of two distinct thrusts in NW India (Valdiya 1980;

61 Saklani *et al.* 1991; Ahmad *et al.* 2000) and in Nepal (Hashimoto *et al.* 1973; Arita 1983; DeCelles

62 *et al.* 2000, Robinson *et al.* 2001; Robinson 2008). In different areas of the belt these two bounding

63 thrusts have been named in different ways, although they seem to refer to the same structural

64 setting. In the Garhwal Himalaya (NW India), the MCTz is well exposed: Valdiya (1980) and

65 Ahmad *et al.* (2000) defined the Munsiari Thrust at the bottom and the Vaikrita Thrust at the top of

66 the MCTz, whereas Saklani *et al.* (1991) defined the lower thrust as MCT2 in the Yamuna valley.

67 The activity time-span of the MCT in different areas of the belt was estimated using mutually

68 contrasting methods or criteria. This span ranges from 23-20 to 15 Ma in different areas of the belt

69   (see Godin *et al.* 2006 and Montomoli *et al.* 2015 for an updated review) down to c. 3 Ma reported

70   in central Nepal (Catlos *et al.* 2001). In the Garhwal Himalaya, several authors proposed their

71   preferred ages of the MCT activity based on different chronometers (K-Ar, Th-Pb and ^{39}Ar-^{40}Ar)

72   and especially on different non-isotopic sample characterisations. Metcalfe (1993) obtained K-Ar

73   ages on biotite and muscovite from the Bhagirathi valley, about 100 km W of our study area (Fig.

74   1a). Based on these data, this author proposed that the MCT was active between 14 and 5.7 Ma.

75   Catlos *et al.* (2002) extended their previous work on Nepal to western Garhwal beneath the Vaikrita

76   Thrust and asserted that the Th-Pb ages of monazite constrain the age of the entire activity of the

77   MCT in the central and western Himalaya to c. 6 Ma. Célérier *et al.* (2009) reported c. 9 Ma

78   obtained using ^{39}Ar-^{40}Ar on muscovite from samples in the middle portion of the MCTz near the

79   village of Helang. Sen *et al.* (2015) obtained ^{40}Ar-^{39}Ar biotite ages of c. 10 Ma and interpreted them

80   as "cooling ages", which were correlated to the exhumation of the GHS caused by MCT thrusting at

81   that time. In addition, muscovite ages of c. 6 Ma were related to a late stage deformation post-dating

82   biotite cooling (Sen *et al.* 2015). However, questions concerning microstructural and chemical

83   features in context with the protracted deformation have not been addressed by any of these

84   conflicting studies.

85   As our observations of the deformation style of the MCTz in Garhwal strongly suggests a more

86   complex history than that described in previous studies, we apply here an integrated structural-

87   microchemical-geochronological approach (Vance *et al.* 2003) to provide a time frame for the

88   different styles of activity of the Vaikrita thrust. The baseline for any interpretation is a detailed

89   microstructural study (e.g. Rolland *et al.* 2009; Montomoli *et al.* 2013, 2015; Iaccarino *et al.*, 2015),

90   which is required to clarify the aforementioned contrasting estimates, as such a study can

91   distinguish between pre-, syn-, and post- kinematic minerals. This can and should be linked to dated

92   minerals applying analytical techniques that allow the recognition of heterochemical phases and

93   simultaneously provide their age (e.g. analyses of monazite by electron microprobe

94   and of mica, amphibole and feldspar by ^{39}Ar-^{40}Ar mass spectrometry: Villa & Williams 2013; Villa

95   & Hanchar 2017).

96   A recognition of heterochemical mineral replacements, and of mineral disequilibria in general, is

97   necessary to take into account the metamorphic reactions and fluid circulation that led to partial

98   resetting and/or growth of new mineral chronometers (Challandes *et al.* 2003, Sanchez *et al.* 2011).

99   The ignorance of the occurrence of several mineral generations must lead (and has led) to

100   inaccurate age estimates. To this end, we report ^{39}Ar-^{40}Ar stepwise heating results on biotite and

101   white-mica separates from very closely spaced mylonitic micaschist samples taken near the Vaikrita

102   Thrust, the structural top of the MCTz. A feature of ^{39}Ar-^{40}Ar dating, most useful for the present

103   study, is its ability to characterise the analysed phases by means of the Cl/K and Ca/K ratios (Müller

104   *et al.* 2002), and thus to diagnose the presence of heterochemical retrogression phases. This is

105   especially valuable when attempting to date fault movements, as sheared minerals are almost

106   always affected by re-crystallisation, dissolution/reprecipitation and alteration, and by resulting

107   grain sizes of a few μm only (Berger *et al.* 2017). This extreme comminution strongly limits the

108   utility of mineral separations, as it, perforce, does not allow us to produce a monomineralic separate

109   and, thus, limits the use of *in-situ* analyses, the spatial resolution of which is often insufficient to

110   obtain results for a single-generation mineral (Müller *et al.* 2002). The impossibility of obtaining

111   monomineralic separates can be circumvented by a judicious use of correlation diagrams (Villa &

112   Hanchar 2017).

113

114   **Geological background of the Himalaya**

115

116   The Himalayan orogen formed by the closure of the Tethyan Ocean and the subsequent collision

117   between India and Asia plates. Even if the timing of terminal collision has been debated in literature

118   (Najman *et al.* 2017 and references therein) the age of collision has been recently constrained by

119   Najman *et al.* (2017) at 54 Ma, at least in the NW portion of the belt. The Himalayan mountain belt

120   is composed of several tectono-metamorphic units bounded by regional scale reverse and normal

121   shear zones (Fig. 1): the Main Frontal Thrust (MFT), the Main Boundary Thrust (MBT), the Main

122   Central Thrust (MCT) and the South Tibetan Detachment System (STDS) (Le Fort 1975). From

123   south to north, the tectonic units of the belt are:

124   (1) The Sub-Himalaya is constituted by Miocene to Pleistocene sediments, derived from the

125   erosion of the belt (Hodges 2000), and delimited at the bottom by the MFT, a tectonic

126   lineament that divides this unit from the underlying undeformed sediments of the Ganga

127   plain. At the top of the Sub-Himalaya, the MBT divides this unit from the upper Lesser

128   Himalayan Sequence (LHS).

129   (2) The LHS (Fig. 1) is made of low to medium grade marble, orthogneiss, quartzite and schist

130   being Lower Proterozoic to Early Palaeozoic in age (Hodges 2000). The MCT, a wide,

131   ductile to brittle, top-to-the south shear zone divides the LHS from the overlying Greater

132   Himalayan Sequence (GHS).

133   (3) The GHS (Fig. 1), representing the metamorphic core of the belt, consists of a sequence of

134   medium- to high-grade Late Proterozoic to Cambrian metamorphic rocks such as gneiss,

135   schist, migmatite, and calc-silicate rocks, which are intruded by Oligocene – Miocene

136   leucogranites named Higher Himalayan Leucogranites (HHL, Visonà *et al.* 2012). The

137   thickness of the GHS is variable (from 2-3 km up to 30 km, Carosi *et al*. 2010, 2014;

138   Montomoli *et al*. 2013). At least two main metamorphic events have been recognized in the

139   GHS: a first Eocene – Oligocene event in the kyanite stability field, characterized by high

140   pressure conditions, and a Miocene event of medium-low pressure conditions (Pognante &

141   Benna 1993; Iaccarino *et al*. 2015 and references therein) in the sillimanite to cordierite

142   stability field. The STDS, a system of normal, ductile to brittle top-to-the north shear zones

143   and faults, divides the GHS from the upper Tethyan Sedimentary Sequence (TSS, Caby *et*

144   *al*. 1983; Burchfiel *et al*., 1992; Carosi *et al*. 1998).

145   (4) The TSS (Fig. 1) comprises Palaeozoic to late Mesozoic low-grade metamorphic and

146   undeformed rocks (Le Fort 1975). The metamorphic grade considerably increases towards

147   the structurally lower portion of the TSS, close to the STDS, up to lower amphibolite facies

148   conditions (Hodges 2000; Dunkl *et al*. 2011; Montomoli *et al*. 2017).

149

150 **Geological framework of the Garhwal Himalaya**

151

152 The study area is located in the Garhwal Himalaya (Uttarakhand, NW India), where a complete

153 structural transect across the MCTz, located between the villages of Helang and Joshimath, has

154 been investigated (Fig. 1a,b). The Munsiari and Vaikrita Thrusts, limiting the MCTz, are shown in

155 Fig. 2a,b,c. The Berinag Formation crops out near Helang, in the southernmost portion of the

156 transect, and belongs to the Lesser Himalayan Sequence (LHS) (Fig. 1b). This formation consists of

157 schist, quartzite and carbonate rock affected by a greenschist-facies metamorphism. The main

158 foliation strikes NW-SE and dips 30-35° to the NE (Fig. 1c, Jain *et al.* 2014).

159 The Munsiari Formation crops out within the MCTz (Fig. 1b), and consists of mylonitic quartzite

160 (Fig. 2a), Precambrian mylonitic orthogneiss (Fig. 2b), garnet-bearing micaschist, and calc-silicate

161 rock (Fig. 1b, Jain *et al.* 2014). The main foliation strikes from W-E to NW-SE and dips 45° from N

162 to NE (Fig. 1d), whereas the main stretching lineation is oriented N20, 45 NE. The main kinematic

163 indicators at the mesoscale (Jain *et al.* 2014) are S-C and S-C-C' fabrics and asymmetrical boudins

164 pointing to a top-to-the S/SW sense of shear (Jain *et al.* 2014). At the microscale, the main

165 kinematic indicators such as S-C fabric, σ and δ porphyroclasts and mica fish confirm a top-to-the-

166 SW sense of shear. At the microscale, the samples of the Vaikrita Thrust show the main foliation

167 (S_m) that overprints an older foliation (S_{m-1}), which is only locally preserved. Garnet is enveloped

168 by the main foliation, whereas staurolite porphyroblasts are syn-kinematic and contain an internal

169 foliation (S_i) concordant with the external one. Grain Boundary Migration (GBM, Passchier &

170 Trouw 2005) and minor-static recrystallisation represent the main deformation mechanisms in

171   quartz. Kinematic indicators such as S-C-C' fabric, mica fish and σ/δ-porphyroclasts indicate a top-

172   to-SW sense of shear (Jain *et al.* 2014).

173   Spencer *et al.* (2012) identified the MCT "*sensu stricto*" with the Vaikrita Thrust (Fig. 2c), a ductile

174   shear zone separating the lower Munsiari Formation from the upper Joshimath Formation belonging

175   to the GHS. Thakur *et al.* (2015) defined the MCTz as a package of sheared rocks bounded by two

176   discrete thrusts, namely the Munsiari Thrust at the bottom and the Vaikrita Thrust at the top,

177   suggesting that the MCTz in the study area corresponds to the Lesser Himalayan Crystalline

178   Sequence (LHCS, Virdi 1986) consisting of low- to medium-grade metamorphic rocks.

179   Spencer *et al.* (2012) and Thakur *et al.* (2015) estimated *P-T* conditions of the MCTz in the study

180   area. The data of these authors agree within the given uncertainties. The former authors used

181   "classical geothermobaric methods" (several cation exchange thermometry and net-transfer

182   reactions barometry) and estimated peak *P-T* conditions between 0.5-1.1 GPa and 500-600° C.

183   Thakur *et al.* (2015) estimated *P-T* conditions of 0.63-0.75 GPa and 550-582° C through

184   pseudosection modeling and multi-equilibrium thermobarometry. Th-Pb monazite as young as c. 6

185   Ma were obtained by Catlos *et al.* (2002) near our study area in Garhwal. However, the age data are

186   decoupled from petrological and textural context, and the overall interpretation remains ambiguous.

187   Sen *et al.* (2015) reported ^{40}Ar-^{39}Ar ages on biotite of c. 10 Ma and on muscovite of c. 6 Ma for

188   rocks from the Vaikrita Thrust.

189   The Joshimath Formation, which forms the lower portion of the GHS in the study area (Fig. 1b, 2d;

190   Spencer *et al.* 2012; Thakur *et al.* 2015), consists of paragneiss, schist, and minor calc-silicate, in

191   which the main foliation strikes from WNW-ESE to NW-SE and dips 35-40° from N to NE (Fig.

192   1e; Jain *et al.* 2014). At the microscale, rocks of the Joshimath Formation show the common

193   mineral assemblage garnet, kyanite, quartz, muscovite, plagioclase, biotite and minor staurolite.

194   According to Thakur et al. (2015), garnet porphyroblasts show inclusions of quartz, biotite and

195   plagioclase.

196   Structurally upward, the Suraithota and Bhapkund Formations (Jain *et al.* 2014) represent the

197   middle and upper GHS in the study area. According to Jain *et al*. (2014), the Suraithota Formation

198   consists of kyanite-garnet-biotite-bearing gneiss, micaschist, quartzite and amphibolite

199   intercalations. The main foliation strikes N120°-150° with a dip of 30°-40° toward NE (Jain *et al*.

200   2014). The Bhapkund Formation includes aluminosilicate-garnet-biotite migmatitic gneiss,

201   tourmaline-rich leucogranitic lenses and dikes, and the Malari leucogranite, a small pluton with an

202   age of c. 19 Ma (U-Pb on zircon, Sachan *et al.* 2010) outcropping at the northern margin of the

203   Bhapkund Formation. According to Sachan *et al.* (2010), the Malari pluton is an undeformed body

204   crosscutting the STDS, whereas Spencer *et al.* (2012), Jain *et al.* (2014), Thakur *et al.* (2015), Sen

205   *et al.* (2015) and Iaccarino *et al.* (2017b) challenged this interpretation. We also found no field

206   evidence that the Malari leucogranite actually crosscuts the STDS.

207

208   **Petrography and microstructures of selected samples**

209

210   Three samples of mylonitic micaschist have been selected from the Vaikrita Thrust close to the

211   village of Tapoban (Fig. 1b, red stars). Sample GW13-29 was collected < 30 m downhill from

212   sample GW13-28, following the road between Joshimath and Suraithota. Sample GW13-29B was

213   taken from the same outcrop, less than 1 m away from GW13-29. All samples display a main

214   schistosity, referred to as S_m, accompanied by variably identifiable rare pre-S_m relics and/or post-S_m

215   static mineral growth.

216   Sample GW13-28 is a garnet-staurolite-two mica-bearing impure quartzite that also contains

217   tourmaline, ilmenite, monazite and abundant late chlorite, partially replacing biotite and garnet (Fig.

218   3b). The main foliation (S_m) is defined by the shape preferred orientation (SPO) of muscovite

219   (muscovite-2), biotite (biotite-2) and ilmenite. This foliation can be classified as disjunctive

220   schistosity characterized by a discrete transition to domains of quartz-rich microlithons. Static

221   recrystallisation of biotite and muscovite can be also sporadically found. In the phyllosilicate-rich

222   layers garnet porphyroclasts are enveloped by the main foliation (Fig. 3a), whereas in the quartz-

223   rich granoblastic domains garnet shows a skeletal aspect. Staurolite appears along the main foliation

224   suggesting a syn-kinematic growth (Fig. 3a). The main recrystallisation mechanism in quartz is

225   GBM supported by sutured and amoeboid grain boundaries (Fig. 3c). However, static annealing of

226   quartz is sometimes discernible by straight grain boundaries and triple points. Kinematic indicators

227   at the microscale are represented by asymmetric recrystallisation tails of micas and asymmetric

228   strain shadows around garnet porphyroclasts (Fig. 3a) and foliation fishes (Fig. 3d; Passchier &

229   Trouw 2005), which show a top-to-the S/SW sense of shear.

230   Sample GW13-29 is a mylonitic micaschist (Fig. 3e,f) with the mineral assemblage quartz, biotite,

231   muscovite, garnet, plagioclase and ilmenite. The S_m is an anastomosing disjunctive schistosity

232   defined by SPO of biotite (biotite-2) and muscovite (muscovite-2). Locally, within the microlithons,

233   micas (micas-1) oriented at high-angle with respect to the S_m mark an older foliation (S_{m-1}, Fig. 3f).

234   Garnet is enveloped by the main foliation and often contains aligned inclusions of quartz,

235   plagioclase, micas and allanitic epidote, defining an internal foliation (S_i) that is non-continuous

236   with the external one (S_e, Fig. 3e). Thus, garnet could be classified as intertectonic porphyroblast.

237   However, in some circumstances inclusions in garnet are not aligned. The mica-2 generation is

238   followed structurally by a static growth of larger mica (mica-3) around garnet grains (Fig. 3e).

239 Additional sporadic mica-3 grains are found in the matrix: they are oriented in the same direction as

240 mica-2 but are not comminuted and suggest later, static growth by a process resembling Ostwald

241 ripening and pseudomorphism. Relict biotite-1 and muscovite-1 may be present but are difficult to

242 identify, as ductile deformation was very intense and has reduced the grain size of mica grains and

243 given them a shredded appearance. The latest generation consists of large micas (muscovite-3 and

244 minor biotite-3) forming coronitic structures around garnet. These micas are characterised by the

245 lack of internal deformation (undulose extinction or kinking) in contrast to mica oriented along S_m.

246 Moreover, static recrystallisation of biotite and muscovite is evident as mica flakes cross-cut S_m.

247 Main deformation mechanisms were GBM followed by minor static recrystallisation of quartz.

248 Asymmetric recrystallisation tails of garnet porphyroclasts indicate a top-to-the-S/SW sense of

249 shear.

250 Sample GW13-29B is a garnet-biotite-bearing mylonitic micaschist (Fig. 3g,h) also containing

251 quartz, muscovite, plagioclase and minor chlorite. The S_m, defined by the SPO of biotite (biotite-2)

252 and muscovite (muscovite-2), can be classified as disjunctive schistosity. The microstructure is

253 characterised by the alternation of granoblastic quartzofeldspathic layers and lepidoblastic layers.

254 The main foliation envelops intertectonic garnet that contains aligned quartz inclusions defining an

255 internal foliation (S_i) discordant to the external one (Fig. 3g,h). Muscovite and biotite crystals

256 (micas-3) show a coronitic texture around garnet porphyroclasts (Fig. 3h). These micas lack

257 undulose extinction, kinking and internal deformation (Fig. 3h). These features are, instead,

258 observed in micas-2 (Fig. 3g,h). Kinematic indicators such as δ-porphyroclasts and prevalent type 1

259 mica fishes (Passchier & Trouw 2005) show a top-to-SW shear sense.

260

261 **Mineral chemistry of micas**

262

263 Electron microprobe (EMP) analyses were carried out with a CAMECA SX100 hosted at the

264 Institut für Mineralogie und Kristallchemie at Universität Stuttgart, equipped with five wavelength-

265 dispersive spectrometers, using an accelerating voltage of 15 kV and a beam current of 10 nA.

266 Details on the analytical protocol are reported in Massonne (2012). Selected analyses of the

267 different structurally-located micas from the studied samples are given in Table 1. Their

268 compositional variabilities are shown in Figures 4 and 5. Muscovite and biotite analyses were

269 recalculated as atoms per formula unit (apfu) on the basis of 11 and 22 oxygens for muscovite and

270 biotite, respectively. Figure 4 displays representative BSE images, in which the variation in X_{Mg}

271 (i.e.,Mg/(Mg+Fe)) and Ti concentration between micas along the main foliation and coronitic micas

272 is highlighted.

273

274   *Muscovite*

275

276   In all three samples, white mica shows a limited compositional variation around the muscovite-

277   celadonite join with Si ranging between 3.05 and 3.17 apfu (Fig. 5a). Muscovite in sample GW13-

278   28 is characterised by Al/Si ratios higher than in the other samples (Fig. 5a). The Ti concentration

279   (Fig. 5b) in muscovite of sample GW13-28 is lower (0.007-0.023 apfu) and less scattered than in

280   samples GW13-29 and GW13-29B. In GW13-29, muscovite-2 contains more Ti (0.030-0.043 apfu)

281   compared to muscovite-3 (0.013-0.030 apfu, Figs. 4 and 5b). The same trend was observed in

282   sample GW13-29B (Fig. 5b), where the Ti contents in muscovite-2 (0.023–0.036 apfu) are,

283   however, only somewhat higher than in mica-3 (0.017-0.035 apfu).

284   The Na/(Na+K) ratio (Guidotti & Sassi 2002; Fig. 5c) of muscovite in sample GW13-28 is higher

285   (c. 0.12-0.14) than in samples GW13-29 and GW13-29B (0.06-0.09), which display similar trends.

286   Muscovite-2 and muscovite-3 from sample GW13-29 have a Na/(Na+K) ratio between 0.06-0.09

287   and 0.06-0.08, respectively. Muscovite-2 and muscovite-3 from sample GW13-29B display similar

288   Na/(Na+K) ratios to those of sample GW13-29 (0.06-0.08: muscovite-2; 0.07-0.08: muscovite-3).

289   The X_{Mg} ratio is lower in muscovite-3 than in muscovite-2. In sample GW13-28 X_{Mg} ranges between

290   0.46 and 0.64. Muscovite-2 in sample GW13-29 shows X_{Mg} values between 0.44 and 0.50, whereas

291   X_{Mg} of muscovite-3 is between 0.39 and 0.47. X_{Mg} in muscovite-2 and muscovite-3 of sample

292   GW13-29B ranges between 0.44 and 0.52 and between 0.40 and 0.51, respectively.

293

294   *Biotite*

295

296   The mass fractions of the three biotite generations are even more lopsided than those of muscovite:

297   biotite-1 and -3 are extremely rare. In sample GW13-28, only biotite-2 was analysed. It shows a

298   remarkable chemical variation (Fig. 5d,e,f); in particular, its X_{Mg} is higher and its Ti mostly lower

299   than that of GW13-29 and GW13-29B. Biotite-2 is fairly homogeneous in GW13-29, whereas it

300   shows two distinct compositional clusters in GW13-29B (Fig. 5d,e,f, green triangles).

301   The Al^{IV} contents of biotite in sample GW13-28 (Fig. 5d) are more variable (2.55-2.87 apfu, Fig.

302   5d) than in biotite-2 and -3 of sample GW13-29 (2.53-2.66 apfu). Biotite from sample GW13-29B

303   forms two compositional clusters discernable in X_{Mg} (0.38-0.40: biotite-2, 0.32-0.34: biotite-3) and

304   Al^{IV} (2.57-2.60 apfu: biotite-2, 2.60-2.68 apfu: biotite-3) plots (Fig. 5d).

305   The Ti concentrations in biotite from sample GW13-28 range between 0.12 and 0.19 apfu, whereas

306   biotite-2 and -3 from sample GW13-29 have higher Ti contents (0.33 -0.36 apfu, except few

9

307   analyses, and 0.22-0.31 apfu, respectively, Fig. 5e). The Ti concentration of biotite-2 in GW13-29

308   is detectably higher than that of GW13-29B (Figs. 4 and 5e).

309   Biotite from sample GW13-29B forms two compositional clusters of biotite-2 discernable in X_{Mg}

310   (0.33-0.34; 0.38-0.40) having the same Ti concentration (c. 0.25-0.29 apfu, Fig. 5e). The six spot

311   analyses having high X_{Mg} all correspond to corroded grains, which might be interpreted as early

312   schistosity-parallel biotite, whereas the other spot analyses with low X_{Mg} correspond to grains with

313   straight grain boundaries.

314   Biotite in sample GW13-29B shows three compositional clusters (Fig. 5e). One corresponds to

315   biotite-3, characterised by Ti contents between 0.18 and 0.30 and X_{Mg} of 0.33-0.35, identical to that

316   of GW13-29. Two correspond to biotite-2, which shows a bimodal chemical composition: one with

317   Ti concentrations between 0.26 and 0.29 apfu and X_{Mg} values of 0.37-0.40 (Fig. 5e) and the other

318   with the same values of the Ti concentration but X_{Mg} values of 0.33-0.34 (Fig. 5e).

319   The K concentrations versus X_{Mg} are shown in Fig. 5f. In sample GW13-28 almost half of the spot

320   analyses yielded low, sub-stoichiometric K (and correspondingly high Al^{IV}) in biotite. These

321   systematic deviations from the other biotite analyses clearly pertain to (partially) altered grains, as

322   supported by the matching element sums below 96 % for these analyses. Both indicators point to a

323   partial replacement by chlorite or smectite and confirm that this sample contains more alteration

324   phases than the others. Both biotite-2 and -3 from sample GW13-29 are characterised by X_{Mg}

325   between 0.32 and 0.35 and K concentrations of 1.82-1.91 apfu.

326

327   **Ti-in-biotite and Ti-in-muscovite geothermometry**

328

329   *Methods*

330

331   Thermal conditions of mica (re-)crystallisation, in regard of the different textural positions

332   described above, were constrained through empirical geothermometers based on the Ti

333   concentration in micas increasing with increasing temperature (Henry *et al.* 2005 and references

334   therein; Chambers & Kohn 2012; Wu & Chen 2015). Henry & Guidotti (2002) and Henry *et al.*

335   (2005), based on an extensive natural biotite dataset from graphite and rutile/ilmenite bearing

336   samples, reconstructed a Ti-saturation surface for biotite of the *P-T* range of 0.4-0.6 GPa and 480-

337   800°C. Based on this saturation surface, they proposed a relationship of between *T* and X_{Mg} and the

338   Ti concentration of biotite, with an associated systematic uncertainty of ±24 °C in the lower *T*

339   range, approaching ±12 °C in the higher *T* calibration range.

10

340   We applied the Ti-in-biotite thermometer proposed by Henry *et al.* (2005). The pressure at which

341   the Ti-in-biotite thermometer was originally calibrated (0.4-0.6 GPa, Henry & Guidotti 2002; Henry

342   *et al.* 2005) is lower than that estimated for rocks that are structurally close to the present ones

343   (0.82-0.88 GPa, Spencer *et al.* 2012; c. 0.73–0.86 GPa, Thakur *et al.* 2015). Therefore, a

344   conservative systematic uncertainty of 50°C on the calculated absolute *T* should be taken into

345   account (e.g. Mottram *et al.* 2014b).

346   The pressure-dependent Ti-in-muscovite thermometer was proposed by Wu & Chen (2015), who

347   empirically calibrated this thermometer for the *P-T* range of 0.1-1.4 GPa and 450-800 °C for

348   ilmenite- and aluminosilicate-satured metapelite. The quoted error of the Ti-in-muscovite

349   thermometer, as suggested by Wu & Chen (2015), is ± 65 °C. We applied the Ti-in-muscovite

350   thermometer, following the assumption of a corresponding equilibrium pressure of 0.8 GPa, in

351   agreement with the *P* estimates previously reported (see above). Calculation at lower P (0.6 GPa)

352   shows only a very minor (around 5 °C) decrease in the *T* estimates. An additional source of bias is

353   the fact that the present rocks do not match the paragenesis used to calibrate the thermometer.

354   Therefore, absolute temperature estimates may be inaccurate, but temperature differences between

355   different mica generations of the same rock are probably accurate (Bucher & Grapes 2011). The Ti-

356   in-biotite and Ti-in-muscovite geothermometers, as any geothermobarometric method (Spear 1993),

357   are not without pitfalls (e.g. Chambers & Kohn 2012), such as, for instance, kinetic problems

358   related to the distance of micas from a Ti source (Waters & Charnley 2002). Moreover,

359   aluminosilicate, required for the Ti-in-muscovite thermometer, is lacking in our samples, even if

360   other Al-rich phases such as garnet and staurolite are present as buffer, so that the Ti-in-muscovite

361   temperature should be regarded as semi-quantitative.

362

363   *Results*

364

365   For muscovite-2, the temperatures obtained with the Ti-in-muscovite thermometer range between

366   394 and 561 °C, 550 and 626 °C, and 591 and 655 °C for sample GW13-28, GW13-29B, and

367   GW13-29, respectively (Fig. S-1). These estimates are similar to, but higher than, those by Spencer

368   *et al.* (2012) and Thakur *et al.* (2015). For samples GW13-28, GW13-29B and GW13-29, the

369   average temperatures are 522±41 °C, 609±15 °C and 632±13 °C, respectively. Average

370   temperatures obtained from muscovite-3 are 538±42 °C for sample GW13-29 and 571±43 °C for

371   sample GW13-29B and, thus, systematically lower than *T* derived from muscovite-2.

372   The Ti-in-biotite geothermometer applied to biotite-2 gave average temperatures of 522±45 °C for

373   sample GW13-28, 647±41 °C for sample GW13-29, and 627±8 °C for sample GW13-29B. The

374   calculated *T* for biotite-3 is 631±18 °C and 607±27 °C for samples GW13-29 and GW13-29B,

375   respectively, somewhat lower than for biotite-2. The obtained temperatures for both muscovite-2

376   and biotite-2 from sample GW13-28 are about 90-100 °C lower than for the other samples. This low

377   temperature estimate parallels the compositional evidence for retrograde reactions (Fig. 5f) and

378   suggests that the chloritization occurred during exhumation at lower *T* (cfr. also Massonne *et al.*

379   2017). In all samples, the calculated temperatures span a large range, which is compatible with a

380   prolonged shearing and recrystallization history. Even taking into account the cautionary notes

381   mentioned above, two factors strengthen our temperature estimates, which are sufficient for the

382   interpretation of ^{39}Ar-^{40}Ar data: (1) the temperatures calculated using two different thermometers

383   match within the corresponding uncertainties and (2) they are similar to the previously reported

384   temperatures of 550-590 °C (Spencer *et al.* 2012; Thakur *et al.* 2015), which are based on the

385   application of several geothermometric methods (e.g. garnet-biotite thermometer, Ti-in-biotite

386   thermometer and multi-equilibrium thermobarometry) for samples in close proximity to the present

387   ones. These temperature estimates are similar to those recorded by fluid inclusions in quartz near

388   the Munsiari Thrust, 1 km downsection (Montemagni *et al.* 2016), namely 500-520 °C.

389

390   **^{39}Ar-^{40}Ar dating**

391

392   *Analytical techniques*

393

394   Mineral separation for samples GW13-28, GW13-29, GW13-29B was performed at the Institut für

395   Geologie at Universität Bern. The rocks were crushed and sieved. Biotite and muscovite in the 150 -

396   350 μm fraction were enriched with gravimetric methods and subsequently purified by extensive

397   hand picking. Density separation of biotite was comparatively straightforward, as biotite is heavier

398   than most major minerals in these rocks. Therefore, most biotite grains in the crushed and sieved

399   sample were included in the separate. On the contrary, muscovite was not efficiently separable by

400   density, and hand-picking was necessary. Only the largest and cleanest-looking grains were chosen.

401   This operator-dependent bias is known to potentially affect samples featuring multiple deformation

402   stages (Villa *et al.* 2014, p. 812). It is therefore expected that the shredded muscovite-2 generation

403   was selectively left out in favour of the nearly-euhedral static muscovite-3 generation.

404   Mica samples were irradiated in the McMaster University Research Reactor (Hamilton, Canada)

405   carefully avoiding Cd shielding. ^{39}Ar-^{40}Ar step-heating analyses were carried out using a double-

406   vacuum resistance furnace attached to a NuInstruments Noblesse™ rare gas mass spectrometer at

407   Dipartimento di Scienze dell'Ambiente e della Terra, Università di Milano Bicocca. The analytical

408   procedure of the ^{39}Ar-^{40}Ar step-heating technique is reported in Villa *et al.* (2000). The irradiation

409   monitor was Fish Canyon sanidine with an assumed age of 28.172 Ma (Rivera *et al.* 2011); the

410   decay constants are those by Steiger & Jäger (1977).

411

412   *Results*

413

414   The first and foremost observation is that all six age spectra (Figs. 6a, 7a) are internally discordant.

415   Even disregarding the steps that clearly do not pertain to mica *sensu stricto* (a first cut off is the

416   Ca/K ratio, which should be lower than 0.03 in micas) the step ages range between 8.6 and 16 Ma

417   for biotite and 3.6 and 7.8 Ma for muscovite. These results are apparently similar to those reported

418   by Sen *et al.* (2015) on nearby samples collected in the Suraithota Formation (Fig. 1a). Moreover,

419   the age pattern featuring older biotite ages and younger muscovite ages is also found in other MCTz

420   localities (Jain, unpublished results; Mottram *et al.* 2015). The latter authors disregarded the biotite

421   ages as due to excess Ar. In contrast, our interpretation of the results exploits the context between

422   microstructural, microchemical and geochronological data and will be presented in the following

423   paragraph.

424

425   **Discussion**

426

427   The remarkable microstructural and chemical complexity of the minerals of the MCTz mylonitic

428   schists requires restricting the following discussion to samples, for which we have established a

429   detailed microstructural and petrogenetic context. It must be pointed out that recent studies (e.g.

430   Berger *et al.* 2017, and references therein) provide conclusive observational evidence that shear-

431   induced recrystallisation is rarely complete and results in extremely small heterochemical relict

432   phases hosted in the recrystallised mineral matrix. In contrast to the interpretation by Sen *et al.*

433   (2015), we will focus on the microstructures and argue that our results reflect a true diachronism.

434   This is made possible by the fact that the selected three samples share the same geological history at

435   the 10 m scale, but record different stages of the microstructural evolution. In the following, we will

436   first focus on the similarities and the differences of the biotite results and then discuss the

437   muscovite results, drawing attention to the observational and interpretive constraints provided by

438   processes affecting biotite. Firstly, it is important to note that the biotite separates analysed here

439   belong to an older mica generation than the muscovite separates. We further propose that discordant

440   steps with low Ca/K and high step ages should be seen as inherited Ar of the sparse relicts of the

441   biotite-1 generation. Therefore, there is no need to invoke excess Ar to explain why biotite-2 is

442   older than muscovite-3. As inherited and excess Ar pertain to two completely different geochemical

443   scenarios (Villa *et al.* 2014, p. 817), namely Ar loss and Ar gain, respectively, neglecting this

444   difference would distort the entire interpretive framework.

445   The biotite age spectra are not only internally discordant (Fig. 6a) but also suggest different Ar

446   retention over an extremely small distance. This indicates that "cooling" (Sen *et al.* 2015) is

447   unlikely to be the only factor controlling the biotite ages. Because age spectra only provide an

448   incomplete information (Chafe *et al.* 2014), it is necessary to also take into account the information

449   provided by the (often neglected) isotopes ^{38}Ar and ^{37}Ar, which are produced from Cl and Ca in the

450   reactor, respectively (Merrihue 1965). From the measured ^{38}Ar/^{39}Ar and ^{37}Ar/^{39}Ar ratios and the

451   known production factors it is possible to calculate the Cl/K and Ca/K ratios, respectively (which

452   can, but need not, be validated by EPM analyses: Villa et al. 2000). Figure 6b shows the Cl/K-Ca/K

453   common-denominator correlation diagram (e.g. Villa & Williams 2013, and references therein).

454   Data-points for all three samples define a very peculiar V-shaped trajectory: the first heating steps

455   of all samples have high Ca/K and high Cl/K ratios, which monitor the degassing of calcium-rich

456   alteration phases. At higher oven temperatures, typical of biotite *sensu stricto* degassing (c. 900 °C),

457   Cl/K and Ca/K ratios reach a minimum and the high-temperature steps show an increase of the

458   Ca/K ratio at constant Cl/K. This pattern applies to biotite from all three samples, but to different

459   degrees. The only way to account for these observations is to hypothesize a three-phase mixture,

460   whereby each sample consists of a different mass fraction of the three end-member phases.

461   Considering the steps most closely matching the Ca-free stoichiometry of biotite, i.e. those with

462   Ca/K < 0.001, it becomes evident that in sample GW13-28 there are none, one in sample GW13-

463   29B, and four in GW13-29. As the micas are fine-grained and intergrown with their retrogression

464   products at a scale < 10 μm, even handpicking cannot achieve a monomineralic separate. In terms

465   of chronological information from biotite, this unexpected observation can be used advantageously,

466   as follows from Fig. 6c. The three biotite separates show a similar, albeit less clearly defined, V-

467   shaped trajectory as in Fig. 6b. The interpretation in terms of a mixture of at least three phases is

468   upheld: the alteration phase(s) having step ages up to 16 Ma and high Ca/K and Cl/K are most

469   abundant in sample GW13-28. The extrapolation of the age-Ca/K trend gives an apparent age > 16

470   Ma. This apparent age is very likely to be geologically meaningless, because of several possible

471   artefacts pertaining to the presence of an alteration phase, such as decoupling of ^{40}Ar and recoiled

472   ^{39}Ar during degassing of fine biotite-chlorite intergrowths (Di Vincenzo *et al.* 2003). Clear evidence

473   for massive chloritisation of biotite GW13-28 is provided by its bulk K concentration of 4.61 %, as

474   calculated from the total ^{39}Ar concentration. This low value attests a clear chloritization of biotite in

475   this separate. Even if the chronological information provided by GW13-28 is meaningless per se, it

476   can provide two kinds of constraints. Firstly, the trend defined by the chloritized biotite exhibits a

477   shallow slope in the Cl/K vs. Ca/K diagram. The observation of a different trend in biotite GW13-

478   29B (higher Cl/K and low, biotite-like Ca/K) suggests the presence of a different biotite generation

479   with a different composition. Permissive evidence for this supposed earlier biotite generation was

480   reviewed above (Fig. 5d). The second type of constraint provided by chloritized biotite GW13-28 is

481   that it can act as a useful end-member on the effect of alteration for the other two biotite separates,

482   which are much less altered but not negligibly so. Indeed, in Fig. 6c the biotite separates GW13-29

483   and 29B follow the same pattern as in Fig. 6b, with one branch of the V-shaped trajectory pointing

484   towards GW13-28. The four steps from GW13-29 (Fig. 6d) corresponding to the lowest Ca/K

485   ratios, i.e. most closely approximating biotite stoichiometry, gave an isochron age of 9.07 ± 0.60

486   Ma (2 sigma uncertainty) with an atmospheric intercept. The atmospheric intercept allows us to

487   consider the average age of these four steps as a legitimate "isochemical age" (Müller *et al.* 2002)

488   of 9.00 ± 0.10 Ma. Strictly speaking, this is a cooling age, as the retention of Ar by biotite is

489   complete only below c. 530 °C (Villa 2015). What is most important here is that biotite-2 formed

490   several Ma earlier than muscovite-3.

491   In contrast to the biotite concentrates, all muscovite separates gave significantly younger ages,

492   between c. 6 and 7 Ma. Age spectra are discordant (Fig. 7a). Muscovite from GW13-28 (the sample

493   with the most altered biotite) shows the most disturbed spectrum with some step ages < 5 Ma, the

494   high Cl/K of which clearly identifies them as the degassing of alteration phases (Fig. 7a). GW 13-

495   29B with the best preserved biotite also shows the least discordant muscovite spectrum. Common

496   regression of the data for muscovite from GW13-29 and -29B in a single Cl/K-age diagram,

497   justified by their spatial proximity (< 1 m) and compositional similarity, reveals a negative

498   correlation (Fig. 7b): a relatively Cl-rich mica with an age $\leq 5.88 \pm 0.03$ Ma, and a Cl-poor one, > 7

499   Ma old. As the microstructural observations distinguish between a fine-grained, shredded

500   muscovite-2 along the main foliation and a coarse-grained, statically grown coronitic muscovite-3,

501   it is very likely that hand-picking did enrich muscovite-3 compared to muscovite-2, but the

502   respective mass fraction of the two generations in our separates are unknown. It is therefore

503   possible that the end-member of the correlation trend seen in Fig. 7b is actually the c. 9 Ma old

504   muscovite-2, if its mass fraction (estimated by mass balance) did not exceed 25 %.

505   An age difference between older biotite and younger muscovite in similar rocks was also observed

506   by Mottram *et al.* (2015) in samples from the MCTz from Sikkim. These authors seem to accept

507   that retention of Ar in muscovite is quite high even if an ambient temperature of 600 °C was

508   maintained over several Ma, as already documented by Di Vincenzo *et al.* (2004), Allaz *et al.*

509   (2011) and Villa *et al.* (2014, p. 817). However, the discussion in Mottram *et al.* (2015), purely

510   based on the assumption of thermally activated Fick's Law diffusion, is internally contradictory, as

511   it fails to explain why biotite is reproducibly older than muscovite, contrary to micas from terrains

512   affected by a static, monometamorphic event (e.g. Allaz *et al.* 2011, and references therein). The

513   exclusive focus on Ar diffusion under the assumption of a static system also forfeits the opportunity

514   to examine microstructures and microchemistry, and correlate both with mica ages.

515   Regarding Ar retention in micas, Villa *et al.* (2014) observed complete, or nearly complete, Ar

516   retention in 100 μm sized phengite in metamorphic terrains at T > 500 °C. Villa (2015) went on to

517   interpolate the retention of Ar in static, monometamorphic biotite and derived a revised Ar "closure

518   temperature" estimate of c. 530 °C, in good agreement with the scarce reliable experimental data

519   (see Villa 2010, 2015). This Ar retentivity is at the lower end of the estimated temperature interval

520   for our Garhwal samples. The implication is that biotite records ages which are not much younger

521   than the metamorphic event at temperatures recorded by Ti-in-biotite and Ti-in-muscovite

522   thermometers (see above). The 9.00 ± 0.10 Ma isochemical age therefore is a cooling age close to

523   the growth of biotite-2 in sample GW13-29. *A fortiori* does the 6 Ma age, inferred from the

524   muscovite correlation diagrams, reflect the static growth (especially considering the updated

525   diffusivity data for muscovite: Villa *et al.* 2014) of muscovite-3 during the subsequent exhumation.

526   Selective sampling bias due to handpicking could account for the observation of Fig. 7b, in which

527   an anticorrelation between two clusters is seen in the Cl/K versus age diagram: muscovite from

528   sample GW13-28 is older and has lower Cl/K (blue dots), whereas younger muscovite from

529   samples GW13-29 and GW13-29B has higher Cl/K (pink and green dots). Mixing relatively Cl-rich

530   static muscovite-3 with Cl-poor muscovite-2 yields a good anticorrelation of age and Cl/K ratio; the

531   age of the foliation-parallel muscovite-2 is higher or equal to the oldest step, in the present case 7.6

532   Ma. By extrapolating the correlation trend towards lower Cl/K values it is possible to infer a

533   muscovite-2 age matching the biotite-2 age of 9 Ma by assuming $Cl/K = 5 \times 10^{-5}$ for muscovite-2.

534   The age of static mica growth is underconstrained, and we can only argue that it was less or equal to

535   the lowest step age of 5.88 ± 0.03 Ma showing the Ca/Cl/K signature of bona fide muscovite.

536   In summary (Fig. 8), syn-tectonic growth of micas-2, defining the main mylonitic foliation at c. 9

537   Ma, constrains the age of shearing along the Vaikrita Thrust. The formation of coronitic micas-3 at

538   5.88 Ma post-dates the deformation due to shearing (Fig. 8) and is related to the advection of K

539   (enabling the growth of K-mica at the expense of garnet), mediated by fluids. The uncommon

540   pattern whereby biotite ages are apparently older than muscovite ages is proposed here to be due to

541   a combination of three causes: (1) the size bias between coronitic muscovite-3 and foliation-

542   forming muscovite-2 caused an artificial enrichment of the larger muscovite-3 grains in the

543   analysed separate; (2) the strong preponderance of muscovite-3 over biotite-3 in the coronites,

544   ensuring that only sporadic large biotite-3 crystals were available for selective hand-picking; and

545   (3) the strong preponderance of biotite-2 over the other biotite generations (biotite-1 and -3)

546   ensuring that a biotite separate would almost exclusively consist of biotite-2.

547   The age of shearing along the two bounding faults of the GHS, namely the MCT and the STDS, can

548   help to discriminate among tectonic models (see Montomoli *et al*. 2013 for a review). Some models

549   require MCT and STDS to be contemporaneous: the *Channel Flow* model (Beaumont *et al*. 2001,

550   2004), the *Wedge Extrusion* model (Hodges *et al*. 1992; Grujic *et al*. 1996; Vannay & Grasemann

551   2001) and the *Wedge Insertion* model (Webb *et al*. 2007). Other models do not necessarily require

552   contemporaneity: the *Critical Taper* model (Platt 1993; Kohn 2008) and the *In-sequence Shearing*

553   model (Carosi *et al*. 2010; Montomoli *et al*. 2013, 2015). The present results argue against

554   contemporaneity. Iaccarino *et al*. (2017b) constrained the ductile shearing along the STDS in the

555   Garhwal region (further N along the same transect of the present study) to between c. 20 and 15 Ma

556   by U-(Th)-Pb *in situ* geochronology on monazite occurring in a high-temperature mylonite. The

557   Bura Buri leucogranite in W Nepal, c. 300 km east of the present area (23-25 Ma old: Carosi *et al*.

558   2013) intruded the TSS and thus provides a clear limit for the termination of the movement along

559   the STDS; the Shivling leucogranite (c. 80 km west of the present area) could represent a similar

560   time limit around 23 Ma (Searle *et al*. 1999, and references therein). In the Yadong region multiple

561   leucogranite intrusions, dated at 23-16 Ma by Liu *et al*. (2017), sealed the STDS at $\geq$ 20 Ma, further

562   supporting the orogen-wide diachroneity of the STDS and MCT.

563

564   **Conclusions**

565

566   1. The MCTz rocks in Garhwal record several well resolvable deformations. Microstructural

567   observations show complex superposition of tectonic foliations, marked by successive mica growth

568   and recrystallisation episodes. Microchemical analyses show both pervasive secondary alteration

569   and primary heterogeneity of biotite. Muscovite is less altered and less clearly heterogeneous.

570   2. Three different generations of micas were observed: mica-1 in a relict foliation at high-angle with

571   respect to the main mylonitic one (S_m); mica-2, oriented along S_m, is characterised by small flakes

572   of both muscovite and biotite; mica-3, consisting of large crystals of muscovite and rare biotite, in

573   coronitic structures around garnet porphyroclasts. Mica-3 lacks undulose extinction; its

574   microstructure and chemical composition suggest formation during retrogression and garnet

575   breakdown.

576   3. ^{39}Ar-^{40}Ar age spectra are discordant and show both inter- and intra-sample discrepancies, which

577   cannot be interpreted as "cooling age" differences, as samples from the same outcrop cooled

578 simultaneously. Instead, Ar systematics reflects sample-specific markers of heterochemical

579 recrystallisation. The isochron age of the Ca-poor steps of biotite separate GW13-29 (i.e. the age of

580 biotite-2) is 9.07 ± 0.60 Ma, corresponding to a weighted isochemical average age of the steps

581 pertaining to biotite *sensu stricto* of 9.00 ± 0.10 Ma. Muscovite shows a negative correlation

582 between the Cl/K ratio and age as a result of a mixture of a relatively Cl-rich mica (muscovite-3),

583 5.88±0.03 Ma old, and a Cl-poor muscovite-2, > 7 Ma old. The extrapolation of the correlation

584 trend to low Cl/K values allows us to suggest, but not to constrain, an end-member (muscovite-2) as

585 old as c. 9 Ma.

586 4. Combining microstructural, microchemical and geochronological data, we propose the following

587 evolution: syntectonic growth of mica-2 occurred along the main foliation at c. 9 Ma; the formation

588 of coronitic muscovite at 5.88 Ma post-dated the deformation due to shearing along the Vaikrita

589 Thrust; minor to pervasive alteration of muscovite occurred before, during and after coronite

590 growth.

591 5. The shearing along the Vaikrita Thrust lasted until at least 9 Ma ago, i.e. continued for 6-7 Ma

592 after the cessation of the movement along the STDS in the same study area.

593

600

601 **References**

602

603 AHMAD, T., HARRIS, N., BICKLE, M., CHAPMAN, H., BUNBORY, J. & PRINCE, C. 2000. Isotopic

604   constraints on the structural relationship between the Lesser Himalayan Series and the High

605   Himalayan Crystalline Series, Garhwal Himalaya. *Geological Society of America Bulletin,* **112**,

606   467-477.

607 ALLAZ, J., ENGI, M., BERGER, A. & VILLA, I. M. 2011. The effects of retrograde reactions and of

608   diffusion on $^{40}Ar–^{39}Ar$ ages of micas. *Journal of Petrology*, **52(4)**, 691-716.

609 ARITA, K., 1983. Origin of the inverted metamorphism of the lower Himalaya, central Nepal.

610   *Tectonophysics*, **95,** 43-60.

611 BEAUMONT, C., JAMIESON, R. A., NGUYEN, M. H., & LEE, B. 2001. Himalayan tectonics explained

612   by extrusion of a low-viscosity crustal channel coupled to focused surface denudation. *Nature*,

613   **414**, 738-742.

614 BEAUMONT, C., JAMIESON, R. A., NGUYEN, M. H., & MEDVEDEV, S. 2004. Crustal channel flows: 1.

615   Numerical models with applications to the tectonics of the Himalayan   Tibetan orogen. *Journal*

616   *of Geophysical Research: Solid Earth*, **109(B6)**.

617 BELTRANDO, M., LISTER, G. S., FORSTER, M., DUNLAP, W. J., FRASER, G., & HERMANN, J. 2009.

618   Dating microstructures by the ^{40}Ar/^{39}Ar step-heating technique: deformation–pressure–

619   temperature–time history of the Penninic units of the Western Alps. *Lithos*, **113(3)**, 801-819.

620 BERGER, A., WEHRENS, P., LANARI, P., ZWINGMANN H. & HERWEGH, M. 2017. Microstructures,

621   mineral chemistry and geochronology of white micas along a retrograde evolution: An example

622   from the Aar massif (Central Alps, Switzerland). *Tectonophysics*, **721**, 179–195.

623 BUCHER, K. & GRAPES, R. 2011. Petrogenesis of metamorphic rocks. *Springer Berlin Heidelberg*.

624 BURCHFIEL, B.C., CHEN, Z., HODGES, K.V., LIU, Y., ROYDEN, L.H., DENG, C., XU, J. 1992. The

625   South Tibetan Detachment System, Himalayan Orogen. *Geological Society of America Special*

626   *Paper*, **269** (41 pp.).

627 CABY, R., PÊCHER, A., LE FORT, P., 1983. Le grand chevauchement central himalayen:Nouvelles

628   données sur le métamorphisme inverse à la base de la Dalle du Tibet. *Revue de Géologie*

629   *Dynamique et de Géographie Physique*, **24**, 89–100.

630 CAROSI, R., GEMIGNANI, L., GODIN, L., IACCARINO, S., LARSON, K., MONTOMOLI, C., RAI, S. M.

631   2014. A geological journey through the deepest gorge on earth: The Kali Gandaki valley section,

632   west-central Nepal. *Journal of the Virtual Explorer*, **47**, paper 7.

633 CAROSI, R., LOMBARDO, B., MOLLI, G., MUSUMECI, G., PERTUSATI, P.C. 1998. The south Tibetan

634   detachment system in the Rongbuk valley, Everest Region. Deformation features and geological

635   implication. *Journal of Asian Earth Sciences,* **16**, 299–311.

636 CAROSI, R., MONTOMOLI, C. & VISONÀ, D. 2002. Is there any detachment in the Lower Dolpo

637   (Western Nepal)? *Comptes Rendus Geoscience*, **334**, 933–940.

638 CAROSI, R., MONTOMOLI, C. & VISONÀ, D. 2007. A structural transect in the Lower Dolpo: insights

639   on the tectonic evolution of Western Nepal. *Journal of Asian Earth Sciences*, **29**, 407-423.

640 CAROSI, R., MONTOMOLI, C., IACCARINO, S., MASSONNE, H. -J., RUBATTO, D., LANGONE, A.,

641   GEMIGNANI, L. & VISONÀ, D. 2016. Middle to late Eocene exhumation of the Greater Himalayan

642   Sequence in the Central Himalayas: Progressive accretion from the Indian plate. *Geological*

643   *Society of America Bulletin*, **128(11-12)**, 1571-1592.

644   CAROSI, R., MONTOMOLI, C., RUBATTO, D. & VISONÀ, D. 2006. Normal-sense shear zones in the

645   core of the Higher Himalayan Crystallines (Bhutan Himalaya): Evidence for

646   extrusion?. *Geological Society, London, Special Publications*, **268**, 425-444.

647   CAROSI, R., MONTOMOLI, C., RUBATTO, D. VISONÀ, D. 2010. Late Oligocene high-temperature

648   shear zones in the core of the Higher Himalayan Crystallines (Lower Dolpo, Western Nepal),

649   *Tectonics*, **29**, TC4029, doi: 10.1029/2008TC002400.

650   CAROSI, R., MONTOMOLI, C., RUBATTO, D., & VISONÀ, D. 2013. Leucogranite intruding the South

651   Tibetan Detachment in western Nepal: implications for exhumation models in the Himalayas.

652   *Terra Nova*, **25(6)**, 478-489.

653   CATLOS, E. J., HARRISON, T. M., MANNING, C. E., GROVE, M., RAI, S. M., HUBBARD, M. S. &

654   UPRETI, B. N. 2002. Records of the evolution of the Himalayan orogen from in situ Th–Pb

655   microprobe dating of monazite: Eastern Nepal and western Garhwal. *Journal of Asian Earth

656   Sciences*, **20**, 459-479.

657   CÉLÉRIER, J., HARRISON, T. M., BEYSSAC, O., HERMAN, F., DUNLAP, W. J. & WEBB, A. A. G. 2009.

658   The Kumaun and Garwhal Lesser Himalaya, India; Part 2. Thermal and deformation histories.

659   *Geological Society of America Bulletin*, **121**, 1281-1297.

660   CHAFE, A. N., VILLA, I. M., HANCHAR, J. M. & WIRTH, R. 2014. A re-examination of petrogenesis

661   and $^{40}Ar/^{39}Ar$ systematics in the Chain of Ponds K-feldspar: "diffusion domain" archetype versus

662   polyphase hygrochronology. *Contributions to Mineralogy and Petrology,* **167**, 1010, doi:

663   10.1007/s00410-014-1010-x.

664   CHALLANDES, N., MARQUER, D. & VILLA, I. M. 2003. Dating the evolution of C–S microstructures:

665   a combined $^{40}Ar/^{39}Ar$ step-heating and UV laserprobe analysis of the Alpine Roffna shear

666   zone. *Chemical Geology*, **197**, 3-19.

667   CHAMBERS, J. A. & KOHN, M. J. 2012. Titanium in muscovite, biotite, and hornblende: Modeling,

668   thermometry, and rutile activities of metapelites and amphibolites. *American

669   Mineralogist*, **97(4)**, 543-555.

670   COTTLE, J. M., SEARLE, M. P., JESSUP, M. J., CROWLEY, J. L. & LAW, R. D. 2015. Rongbuk re-

671   visited: Geochronology of leucogranites in the footwall of the South Tibetan Detachment

672   System, Everest Region, Southern Tibet. *Lithos*, 227, 94-106, doi:

673   http://dx.doi.org/10.1016/j.lithos.2015.03.019.

674   DECELLES, P. G., GEHRELS, G. E., QUADE, J., LAREAU, B. & SPURLIN, M. 2000. Tectonic

675   implications of U–Pb zircon ages of the Himalayan orogenic belt in Nepal. *Science*, **288**, 497-

676   499.

677 DI VINCENZO, G., CAROSI, R. & PALMERI, R. 2004. The relationship between tectono-metamorphic

678   evolution and argon isotope records in white mica: constraints from in situ ^{40}Ar–^{39}Ar laser

679   analysis of the Variscan basement of Sardinia. *Journal of Petrology*, *45*, 1013-1043.

680 DI VINCENZO, G., VITI, C., & ROCCHI, S. 2003. The effect of chlorite interlayering on 40Ar–39Ar

681   biotite dating: an ^{40}Ar–^{39}Ar laser-probe and TEM investigations of variably chloritised biotites.

682   *Contributions to Mineralogy and Petrology*, **145(6)**, 643-658.

683 DUNKL, I., ANTOLÍN, B., WEMMER, K., RANTITSCH, G., KIENAST, M., MONTOMOLI, C., DING, L.,

684   CAROSI, R., APPEL, E., EL BAY, R., XU, Q., & VON EYNATTEN, H. 2011. Metamorphic evolution

685   of the Tethyan Himalayan flysch in SE Tibet. In: Growth and Collapse of the Tibetan Plateau.

686   Eds. Gloaguen R., Ratschbacher L., *Geological Society of London Special Publications*, **353**: 45-

687   69.

688 GIBSON, R., GODIN, L., KELLETT, D. A., COTTLE, J. M. & ARCHIBALD, D. 2016. Diachronous

689   deformation along the base of the Himalayan metamorphic core, west-central Nepal. *Geological*

690   *Society of America Bulletin*, **128**, 860-878.

691 GODIN, L., GRUJIC, D., LAW, R. D. & SEARLE, M. P. 2006.Channel flow, ductile extrusion and

692   exhumation in continental collision zones: an introduction. *In*: Law, R. D., Searle, M. P. &

693   Godin, L. (eds) *Channel Flow, Ductile Extrusion and Exhumation in Continental Collision*

694   *Zones*. Geological Society, London, Special Publications, **268**, 1–23.

695 GRUJIC, D., CASEY, M., DAVIDSON, C., HOLLISTER, S.L., KÜNDIG, R., PAVLIS, T., & SCHMID, S.

696   1996. Ductile extrusion of the Higher Himalayan Crystalline in Bhutan: evidence from quartz

697   microfabrics. *Tectonophysics*, **260**, 21–43.

698 GUIDOTTI, C.V. & SASSI F. P. 2002. Constraints on studies of metamorphic K-Na white micas. In:

699   Micas: Crystal Chemistry & Metamorphic Petrology, *Reviews in Mineralogy and Geochemistry,*

700   **46***, 413-448.

701 HASHIMOTO, S., OHTA, Y. & AKIBA, C. lY73. Geology of the Nepal Himalayas. Saikon, Tokyo. 286

702   pp.

703 HEIM, A. A. & GANSSER, A. 1939. Central Himalaya: Geological observations of the Swiss

704   Expedition, 1936. *Delhi, India, Hindustan Publishing*, pp. 26.

705 HENRY, D. J., & GUIDOTTI, C. V. 2002. Titanium in biotite from metapelitic rocks: Temperature

706   effects, crystal-chemical controls, and petrologic applications. *American Mineralogist*, **87(4)**,

707   375-382.

708 HENRY, D. J., GUIDOTTI, C. V. & THOMSON, J. A. 2005. The Ti-saturation surface for low-to-

709   medium pressure metapelitic biotites: Implications for geothermometry and Ti-substitution

710   mechanisms. *American Mineralogist*, **90(2-3)**, 316-328.

711   HODGES, K.V. 2000. Tectonics of the Himalaya and southern Tibet from two perspectives.

712   *Geological Society of America Bulletin*, **112**, 324-350.

713   HODGES, K.V., PARRISH, R.R., HOUSH, T.B., LUX, D.R., BURCHFIEL, B.C., ROYDEN, L.H., & CHEN,

714   Z. 1992. Simultaneous Miocene extension and shortening in the Himalayan Orogen. *Science*,

715   **258**, 1466–1470.

716   IACCARINO, S., MONTOMOLI, C., CAROSI, R., MASSONNE, H.-J. & VISONÀ, D. 2017a. Geology and

717   tectono-metamorphic evolution of the Himalayan metamorphic core: insights from the Mugu

718   Karnali transect, Western Nepal (Central Himalaya). *Journal of Metamorphic Geology*, **35**, 301-

719   325, doi:10.1111/jmg.12233.

720   IACCARINO, S., MONTOMOLI, C., CAROSI, R., MASSONNE, H.-J., LANGONE, A. & VISONÀ, D. 2015.

721   Pressure–temperature–time–deformation path of kyanite-bearing migmatitic paragneiss in the

722   Kali Gandaki valley (Central Nepal): Investigation of Late Eocene–Early Oligocene melting

723   processes. *Lithos,* **231**, 103-121.

724   IACCARINO, S., MONTOMOLI, C., CAROSI, R., MONTEMAGNI, C., MASSONNE, H.-J., LANGONE, A.,

725   JAIN, A.K., VISONÀ, D. 2017b. Pressure-Temperature-Deformation-Time constraints on the

726   South Tibetan Detachment System in Garhwal Himalaya (NW India). *Tectonics,* **36**, 2281-2304,

727   doi: 10.1002/2017TC004566.

728   JAIN, A. K., SHRESHTHA, M., SETH, P., KANYAL, L., CAROSI, R., MONTOMOLI, C., IACCARINO, S. &

729   MUKHERJEE, P. K. 2014. The Higher Himalayan Crystallines, Alaknanda – Dhauli Ganga

730   Valleys, Garhwal Himalaya, India. *In*: Montomoli, C., Carosi, R., Law, R., Singh, S. & Rai, S.M.

731   (eds) *Geological field trips in the Himalaya, Karakoram and Tibet*. Journal of the Virtual

732   Explorer Electronic Edition, **47**, paper 8.

733   KELLETT, D. A., WARREN, C., LARSON, K. P., ZWINGMANN, H., VAN STAAL, C. R., & ROGERS, N.

734   (2016). Influence of deformation and fluids on Ar retention in white mica: Dating the Dover

735   Fault, Newfoundland Appalachians. *Lithos*, **254**, 1-17.

736   KOHN, M. J. 2008. P T t data from Nepal support critical taper and repudiate large channel flow

737   of the Greater Himalayan Sequence. *Geological Society of America Bulletin*, **120**, 259–273.

738   LE FORT, P. 1975. Himalayas: the collided range. Present knowledge of the continental

739   arc. *American Journal of Science*, **275**, 1-44.

740   LIU, Z. C., WU, F. Y., QIU, Z. L., WANG, J. G., LIU, X. C., JI, W. Q., & LIU, C. Z. 2017. Leucogranite

741   geochronological constraints on the termination of the South Tibetan Detachment in eastern

742   Himalaya. *Tectonophysics (in press)*, doi:10.1016/j.tecto.2017.08.019.

743   MARTIN, A. J. 2016. A review of definitions of the Himalayan Main Central Thrust. *International*

744   *Journal of Earth Science*, doi:10.1007/s00531-016-1419-8.

745 MARTIN, A. J., DECELLES, P. G., GEHRELS, G. E., PATCHETT, P. J. & ISACHSEN, C. 2005. Isotopic

746   and structural constraints on the location of the Main Central thrust in the Annapurna Range,

747   central Nepal Himalaya. *Geological Society of America Bulletin,* **117**, 926-944.

748 MASSONNE, H.-J. 2012. Formation of amphibole and clinozoisite–epidote in eclogite owing to fluid

749   infiltration during exhumation in a subduction channel. *Journal of Petrology*, **53(10)**, 1969-1998.

750 MASSONNE, H.-J., CRUCIANI, G., FRANCESCHELLI, M., & MUSUMECI, G. 2017. Anti clockwise

751   pressure temperature paths record Variscan upper plate exhumation: example from

752   micaschists of the Porto Vecchio region, Corsica. *Journal of Metamorphic Geology*, doi:

753   10.1111/jmg.12283.

754 MERRIHUE, C. M. 1965. Trace-element determinations and potassium-argon dating by mass

755   spectroscopy of neutron-irradiated samples. *Transactions of the American Geophysical*

756   *Union*, **46**, 125.

757 METCALFE, R. P. 1993. Pressure, temperature and time constraints on metamorphism across the

758   Main Central Thrust zone and High Himalayan Slab in the Garhwal Himalaya. *Geological*

759   *Society, London, Special Publications*, **74(1)**, 485-509.

760 MONTEMAGNI, C., FULIGNATI, P., IACCARINO, S., MARIANELLI, P., MONTOMOLI, C. & SBRANA, A.

761   2016. Deformation and fluid flow in the Munsiari Thrust (NW India): a preliminary fluid

762   inclusion study. *Atti Società Toscana Scienze Naturali*, **123**, 67-77, doi:

763   10.2424/ASTSN.M.2016.22.

764 MONTOMOLI, C., CAROSI, R. & IACCARINO, S. 2015. Tectonometamorphic discontinuities in the

765   Greater Himalayan Sequence: a local or a regional feature? *In*: Mukherjee, S., van der Beek, P.

766   & Mukherjee, P.K. (eds) *Tectonics of the Himalaya*. Geological Society, London, Special

767   Publications, **412**, 21-41, doi: 10.1144/SP412.3.

768 MONTOMOLI, C., IACCARINO, S., ANTOLIN, B., APPLE, E., CAROSI, R., DUNKL, I., DING, L., VISONÀ,

769   D. 2017. Tectono-metamorphic evolution of the Tethyan Sedimentary Sequence (Himalayas, SE

770   Tibet). *Italian Journal of Geosciences*, **136**: 73-88, doi: 10.3301/IJG.2015.42.

771 MONTOMOLI, C., IACCARINO, S., CAROSI, R., LANGONE, A. & VISONÀ, D. 2013.

772   Tectonometamorphic discontinuities within the Greater Himalayan Sequence in Western Nepal

773   (Central Himalaya): Insights on the exhumation of crystalline rocks. *Tectonophysics*, **608**, 1349-

774   1370.

775 MOTTRAM, C. M., ARGLES, T. W., HARRIS, N. B. W., PARRISH, R. R., HORSTWOOD, M. S. A.,

776   WARREN, C. J. & GUPTA, S. 2014a. Tectonic interleaving along the Main Central Thrust, Sikkim

777   Himalaya. *Journal of the Geological Society,* **171**, 255–268.

778 MOTTRAM, C. M., PARRISH, R. R., REGIS, D., WARREN, C. J., ARGLES, T. W., HARRIS, N. B. &

779   ROBERTS, N. M. 2015. Using U Th Pb petrochronology to determine rates of ductile thrusting:

780   Time windows into the Main Central Thrust, Sikkim Himalaya. *Tectonics*, **34**, 1355-1374.

781 MOTTRAM, C. M., WARREN, C. J., REGIS, D., ROBERTS, N. M., HARRIS, N. B., ARGLES, T. W. &

782   PARRISH, R. R. 2014b. Developing an inverted Barrovian sequence; insights from monazite

783   petrochronology. *Earth and Planetary Science Letters*, **403**, 418-431.

784 MUKHOPADHYAY, D. K., CHAKRABORTY, S., TREPMANN, C., RUBATTO, D., ANCZKIEWICZ, R.,

785   GAIDIES, F., DASGUPTA, S. & CHOWDHURY, P. 2017. The nature and evolution of the Main

786   Central Thrust: Structural and geochronological constraints from the Sikkim Himalaya, NE

787   India. *Lithos*, doi:10.1016/j.lithos.2017.01.015.

788 MÜLLER, W., KELLEY, S. P. & VILLA, I. M. 2002. Dating fault-generated pseudotachylytes:

789   Comparison of ^{40}Ar/^{39}Ar stepwise-heating, laser-ablation and Rb-Sr microsampling

790   analyses. *Contributions to Mineralogy and Petrology*, **144**, 57-77.

791 NAJMAN, Y., JENKS, D., GODIN, L., BOUDAGHER-FADEL, M., MILLAR, I., GARZANTI, E.,

792   HORSTWOOD, M., & BRACCIALI, L. 2017. The Tethyan Himalayan detrital record shows that

793   India–Asia terminal collision occurred by 54 Ma in the Western Himalaya. *Earth and Planetary*

794   *Science Letters*, **459**, 301-310.

795 PARSONS, A. J., LAW, R. D., LLOYD, G. E., PHILLIPS, R. J. & SEARLE, M. P. 2016. Thermo-kinematic

796   evolution of the Annapurna-Dhaulagiri Himalaya, central Nepal: the Composite Orogenic

797   System. *Geochemistry, Geophysics, Geosystems*, **17**, 1511-1539.

798 PASSCHIER, C. W. & TROUW, R. A. J. 2005. Microtectonics. *Second Edition. Springer, Berlin.*

799 PLATT, J. P. 1993. Exhumation of high-pressure rocks: a review of concept and processes. *Terra*

800   *Nova*, **5**, 119–133.

801 POGNANTE, U. & BENNA, P. 1993. Metamorphic zonation, migmatization and leucogranites along

802   the Everest transect of eastern Nepal and Tibet: record of an exhumation history. *Geological*

803   *Society, London, Special Publications*, **74(1)**, 323-340.

804 RIVERA, T. A., STOREY, M., ZEEDEN, C., HILGEN, F. J., & KUIPER, K. 2011. A refined astronomically

805   calibrated ^{40}Ar/^{39}Ar age for Fish Canyon sanidine. *Earth and Planetary Science Letters*, **311(3)**,

806   420-426.

807 ROBINSON, D. M. 2008. Forward modeling the kinematic sequence of the central Himalayan thrust

808   belt, western Nepal. *Geosphere*, **4**, 785-801.

809 ROBINSON, D. M., DECELLES, P. G., GARZIONE, C. N., PEARSON, O. N., HARRISON, T. M. &

810   CATLOS, E. J. 2001. The kinematic evolution of the Nepalese Himalaya interpreted from Nd

811   isotopes. *Earth and Planetary Science Letters*, **192**, 507-521.

812 ROLLAND, Y., COX, S. F. & CORSINI, M. 2009. Constraining deformation stages in brittle–ductile

813   shear zones from combined field mapping and ^{40}Ar/^{39}Ar dating: the structural evolution of the

814   Grimsel Pass area (Aar Massif, Swiss Alps). *Journal of Structural Geology*, **31**, 1377-1394.

815 SACHAN, H. K., KOHN, M. J., SAXENA, A. & CORRIE, S. L. 2010. The Malari leucogranite, Garhwal

816   Himalaya, northern India: chemistry, age, and tectonic implications. *Geological Society of*

817   *America Bulletin*, **122**, 1865-1876.

818 SAKLANI, P. S., NAINWAL, D. C. & SINGH, V. K. 1991. Geometry of the composite Main Central

819   Thrust (MCT) in the Yamuna Valley, Garhwal Himalaya, India. *Neues Jahrbuch für Geologie*

820   *und Palaeontologie: Monatshefte*, **6**, 364-380.

821 SANCHEZ, G., ROLLAND, Y., SCHNEIDER, J., CORSINI, M., OLIOT, E., GONCALVES, P., VERATI, C.,

822   LARDEAUX, J. -M. & MARQUER, D. 2011. Dating low-temperature deformation by ^{40}Ar/^{39}Ar on

823   white mica, insights from the Argentera-Mercantour Massif (SW Alps). *Lithos*, **125**, 521-536.

824 SEARLE, M. P., LAW, R. D., GODIN, L., LARSON, K. P., STREULE, M. J., COTTLE, J. M. & JESSUP,

825   M. J. 2008. Defining the Himalayan Main Central Thrust in Nepal. *Journal of the Geological*

826   *Society, London*, **165,** 523-534.

827 SEARLE, M. P., NOBLE, S. R., HURFORD, A. J., & REX, D. C. 1999. Age of crustal melting,

828   emplacement and exhumation history of the Shivling leucogranite, Garhwal Himalaya.

829   *Geological Magazine*, **136**, 513-525.

830 SEN, K., CHAUDHURYA, R. & PFÄNDER, J. 2015. ^{40}Ar–^{39}Ar age constraint on deformation and

831   brittle–ductile transition of the Main Central Thrust and the South Tibetan Detachment zone

832   from Dhauliganga valley, Garhwal Himalaya, India. *Journal of Geodynamics*, **88**, 1-13.

833 SPEAR, F. S. 1993. Metamorphic Phase Equilibria and Pressure- Temperature-Time Paths.

834   Mineralogical Society of America, Washington, DC, 799 pp.

835 SPENCER, C. J., HARRIS, R. A. & DORAIS, M. J. 2012. The metamorphism and exhumation of the

836   Himalayan metamorphic core, eastern Garhwal region, India. *Tectonics*, **31**, 1-18.

837 STEIGER, R., & JÄGER, E. 1977. Subcommission on geochronology: convention on the use of decay

838   constants in geo-and cosmochronology. *Earth and planetary science letters*, **36**, 359-362.

839 THAKUR, S. S., PATEL, S. C. & SINGH, A. K. 2015. A P-T pseudosection modelling approach to

840   understand metamorphic evolution of the Main Central Thrust Zone in the Alaknanda valley,

841   NW Himalaya. *Contribution to Mineralogy and Petrology*, **170**, 1-26.

842 VALDIYA, K. S. 1980. The two intracrustal boundary thrusts of the Himalaya. *Tectonophysics*, **66**,

843   323-348.

844 VANCE, D., MÜLLER, W. & VILLA, I. M. (2003). Geochronology: linking the isotopic record with

845   petrology and textures—an introduction. In: Vance, D., Müller, W. & Villa, I. M. (eds)

846   *Geochronology: Linking the Isotopic Record with Petrology and Textures*. Geological Society,

847   London, Special Publications, **220**, 1-24.

848   VANNAY, J.C. & GRASEMANN, B. 2001. Himalayan inverted metamorphism and synconvergence

849   extension as a consequence of a general shear extrusion. *Geological Magazine*, **138**, 253–276.

850   VILLA, I. M. & HANCHAR, J.M. 2017. Age discordance and mineralogy. *American Mineralogist,*

851   doi: 10.2138/am-2017-6084.

852   VILLA, I. M. & WILLIAMS, M. L. 2013. Geochronology of metasomatic events. In: Harlov, D. E. &

853   Austrheim, H. (eds) *Metasomatism and the Chemical Transformation of Rock*. Springer,

854   Heidelberg, pp. 171–202.

855   VILLA, I. M. 2010. Disequilibrium textures versus equilibrium modelling: geochronology at the

856   crossroads. *Geological Society, London, Special Publications*, **332**, 1-15.

857   VILLA, I. M. 2015. ^{39}Ar-^{40}Ar geochronology of mono-and polymetamorphic basement

858   rocks. *Periodico di mineralogia*, **84**, 615-632.

859   VILLA, I. M., BUCHER, S., BOUSQUET, R., KLEINHANNS, I.C. & SCHMID, S.M. 2014. Dating

860   polygenetic metamorphic assemblages along a transect across the Western Alps. *Journal of*

861   *Petrology*, **55**, 803-830.

862   VILLA, I. M., HERMANN, J., MÜNTENER, O. & TROMMSDORFF, V. 2000. ^{39}Ar– ^{40}Ar dating of

863   multiply zoned amphibole generations (Malenco, Italian Alps). *Contributions to Mineralogy and*

864   *Petrology*, **140(3)**, 363-381.

865   VIRDI, N. S. 1986. Lithostratigraphy and structure of Central Crystallines in the Alaknanda and

866   Dhauliganga valleys of Garhwal U.P. Himalayan thrusts and associated rocks. In: Saklani, P. S.

867   (eds) *Current trends in geology*, **10**, 155–166.

868   VISONÀ, D., CAROSI, R., MONTOMOLI, C., PERUZZO, M. & TIEPOLO, L. 2012. Miocene andalusite

869   leucogranite in central-east Himalaya (Everest–Masang Kang area): low-pressure melting during

870   heating. *Lithos*, **144**, 194-208.

871   WATERS, D. J. & CHARNLEY, N. R. 2002. Local equilibrium in polymetamorphic gneiss and the

872   titanium substitution in biotite. *American Mineralogist*, **87(4)**, 383-396.

873   WEBB, A. A. G., YIN, A., HARRISON, T. M., CÉLÉRIER, J. & BURGESS, W. P. 2007. The leading edge

874   of the Greater Himalayan Crystalline complex revealed in the NW Indian Himalaya:

875   implications for the evolution of the Himalayan orogen. *Geology*, **35**, 955-958.

876   WEBB, A. A. G., YIN, A. & DUBEY, C. S. 2013. U-Pb zircon geochronology of major lithologic units

877   in the eastern Himalaya: implications for the origin and assembly of Himalayan rocks.

878   *Geological Society of America Bulletin,* **125**, 499-522.

879 WEINBERG, R. F. 2016. Himalayan leucogranites and migmatites: nature, timing and duration of

880 anatexis, *Journal of Metamorphic Geology,* **34***,* 821-843.

881 WU, C. M. & CHEN, H. X. 2015. Calibration of a Ti-in-muscovite geothermometer for ilmenite-and

882 Al_2SiO_5-bearing metapelites. *Lithos*, **212**, 122-127.

883

884 **Figure captions**

885

886 Fig. 1: simplified geological map of (a) the Himalayas after Weinberg (2016) and (b) study area

887 (after Jain *et al.* 2014). Red stars indicate the position of analysed samples. Sterographic projections

888 (Wulff net, lower hemisphere) refer to main foliation measured in the different tectonic units: (c)

889 the Lesser Himalayan Sequence, (d) the MCTz and (e) the Joshimath Formation from Jain *et al*.

890 (2014).

891

892 Fig. 2: (a), (b) outcrops of the pervasively sheared rocks of the MCTz near the Munsiari Thrust, in

893 which the kinematic indicators point a top-to-the-SW sense of shear (a) mylonitic impure marble

894 with millimetric mica fish and asymmetrically deformed quartz porphyroclasts; (b) mylonitic

895 orthogneiss with asymmetric tails around feldspar porphyroclasts; (c) outcrop of the Vaikrita Thrust

896 with mylonitic micaschist interbedded with quartzitic levels showing top-to-the-SW sense of shear;

897 (d) garnet-kyanite bearing paragneiss of the Joshimath Formation.

898

899 Fig. 3: microstructures of the Vaikrita Thrust. (a) garnet porphyroclast wrapped by the main

900 foliation (S_m) , showing a top-to-the-SW sense of shear (sample GW13-28); (b) chloritization of

901 biotite (sample GW13-28); (c) ameboid grain boundaries in quartz, testifying GBM recrystallization

902 (sample GW13-28); (d) foliation fish pointing a top-to-SW sense of shear (GW13-28); (e) δ-type

903 garnet porphyroclasts in sample GW13-29 showing a top-to-SW shear sense. Note the coronitic

904 micas-3 around garnet; (f) S_m and relict S_{m-1} in mylonitic micaschist (sample GW13-29); (g) δ-type

905 garnet porphyroclast, displaying a top-to-SW sense of shear, (sample GW13-29B); (h) detail of the

906 inset in Fig. 3g. Note non-deformed coronitic micas and deformed micas on the S_m, intertectonic

907 garnet shows a S_i discordant with respect to the S_m (sample GW13-29B). Mineral abbreviations: Bt

908 – biotite, Grt – garnet, Qz– quartz, St – staurolite, Tur – torumaline, Ms - muscovite.

909

910 Fig. 4: representative BSE images with X_{Mg} value (bold) and Ti apfu concentration (italic) in white

911 for muscovite and in yellow for biotite. (a), (b): sample GW13-28; (c), (d): sample GW13-29; (e),

27

707   Fig. 4: (a) ^{39}Ar-^{40}Ar age spectra of biotite comparing the three samples of the Vaikrita Thrust; (b)

708   V-shaped trajectory of Cl/K vs Ca/K diagram. In the black box are highlighted the reliable low Ca –

709   low Cl analyses, the dashed lines represent two trends: low Cl – variable Ca of the alteration phases

710   of sample GW13-28 and variable Cl – low Ca trend; (c) age vs Cl/K correlation diagram of sample

711   GW13-29 and GW13-29B. The dotted line contains the reliable analyses; (d) isochron obtained

712   with the best four steps of sample GW13-29, corresponding to analyses contained in the dotted

713   circle in (c).

714

715   Fig. 5: (a) ^{39}Ar-^{40}Ar age spectra of muscovite comparing the three samples of the Vaikrita Thrust.

716   (b) Age vs Cl/K correlation diagram reveals a negative correlation between a Cl-rich mica,

717   representing the coronitic white mica, and a Cl-poor one, possibly representing white mica along

718   the S_p. Musc-2 – white mica along the Sp; Musc-3 – coronitic white mica around garnet.

719

720   Fig. S-1: histograms reporting thermometric data obtained with Ti-in-biotite and Ti-in-muscovite

721   geothermometers. (a) and (c): data on white mica along the S_p (white mica-2) and coronitic around

722   garnet (white mica-3), respectively; (b) and (d) data on biotite along the S_p (biotite-2) and coronitic

723   around garnet (biotite-3), respectively. The legend in (b-d) is the same in (a).

724

725   **Table captions**

726

727   Table 1: representative electron microprobe analyses of white mica and biotite

728

729   Supplementary Table 1: ^{39}Ar-^{40}Ar data

Table 1

	Sample 28						Sample 29								Sample 29B							
	Muscovite			Biotite			Muscovite				Biotite				Muscovite				Biotite			
	Sp	Sp	Sp	Sp	Sp	Sp	cor.	cor.	Sp	Sp	cor.	cor.	Sp	Sp	cor.	cor.	Sp	Sp	cor.	cor.	Sp	Sp
SiO_2	46.14	46.27	46.00	34.36	34.98	33.54	45.37	46.09	45.79	45.64	34.28	34.28	34.60	34.50	44.98	46.17	45.62	45.13	33.99	34.31	34.13	35.00
TiO_2	0.44	0.45	0.39	1.52	1.27	1.55	0.49	0.29	0.77	0.79	2.48	2.36	3.07	3.04	0.33	0.47	0.72	0.68	1.56	1.86	2.33	2.52
Al_2O_3	33.79	34.06	33.85	18.82	18.93	19.16	33.46	33.93	32.42	32.41	17.27	17.15	17.24	16.90	33.98	34.26	33.08	32.77	18.16	17.47	17.40	17.91
FeO_{tot}	1.41	1.01	1.12	21.69	20.86	21.14	2.04	1.91	2.26	2.22	23.15	23.22	23.23	23.07	1.97	1.99	2.19	2.19	24.39	24.47	24.13	22.19
MnO	b.d.	b.d.	b.d.	0.05	0.04	0.01	b.d.	0.01	b.d.	b.d.	0.16	0.15	0.18	0.12	0.01	b.d.	0.01	b.d.	0.07	0.01	0.07	b.d.
MgO	1.06	0.91	1.00	8.82	8.64	9.78	0.83	0.89	1.18	1.08	6.67	6.86	6.87	6.84	0.77	0.91	1.05	1.04	7.22	7.11	6.90	8.04
CaO	b.d.	b.d.	0.01	b.d.	0.03	0.03	b.d.	0.01	b.d.	b.d.	0.01	0.01	b.d.	b.d.	0.02	b.d.	b.d.	b.d.	b.d.	0.01	b.d.	b.d.
BaO	0.19	0.13	0.19	0.11	0.05	0.06	0.30	0.27	0.31	0.31	0.15	0.13	0.15	0.25	0.24	0.24	0.21	0.21	0.10	0.13	0.18	0.20
Na_2O	0.90	0.92	0.91	0.07	0.28	0.06	0.59	0.65	0.54	0.56	0.13	0.08	0.16	0.15	0.58	0.62	0.62	0.49	0.09	0.09	0.07	0.08
K_2O	10.21	9.68	10.01	8.96	9.38	7.59	10.92	10.66	10.97	10.39	9.44	9.58	9.27	9.61	10.90	10.88	10.82	10.71	9.41	9.74	9.72	9.74
F	b.d.	0.05	0.09	0.29	0.38	0.18	0.05	b.d.	0.17	0.05	0.21	0.25	0.13	0.15	b.d.	b.d.	b.d.	0.08	0.28	0.04	0.19	0.24
Cl	b.d.	0.01	b.d.	0.04	0.12	0.04	b.d.	b.d.	b.d.	b.d.	0.03	0.02	0.02	0.02	0.01	b.d.	b.d.	0.01	0.03	0.03	0.02	0.03
Tot	94.15	93.49	93.58	94.73	94.94	93.13	94.05	94.70	94.42	93.44	93.96	94.08	94.92	94.65	93.79	95.53	94.31	93.32	95.30	95.25	95.15	95.96
Si	3.12	3.13	3.12	5.33	5.39	5.24	3.09	3.11	3.12	3.13	5.43	5.43	5.42	5.43	3.07	3.09	3.10	3.10	5.33	5.40	5.37	5.39
Ti	0.02	0.02	0.02	0.18	0.15	0.18	0.03	0.01	0.04	0.04	0.30	0.28	0.36	0.36	0.02	0.02	0.04	0.04	0.18	0.22	0.28	0.29
Al	2.69	2.71	2.70	3.44	3.44	3.53	2.69	2.70	2.60	2.62	3.23	3.20	3.18	3.14	2.74	2.70	2.65	2.65	3.36	3.24	3.23	3.25
Fe	0.08	0.06	0.06	2.81	2.69	2.76	0.12	0.11	0.13	0.13	3.07	3.08	3.04	3.04	0.11	0.11	0.12	0.13	3.20	3.22	3.18	2.86
Mn	--	--	--	0.01	0.00	0.00	--	0.00	--	--	0.02	0.02	0.02	0.02	0.00	--	0.00	--	0.01	0.00	0.01	--
Mg	0.11	0.09	0.10	2.04	1.98	2.28	0.08	0.09	0.12	0.11	1.57	1.62	1.60	1.61	0.08	0.09	0.11	0.11	1.69	1.67	1.62	1.85
Ca	--	--	0.00	--	0.00	0.01	--	0.00	--	--	0.00	0.00	--	--	0.00	--	--	--	--	0.00	--	--
Ba	0.00	0.00	0.01	0.01	0.00	0.00	0.01	0.01	0.01	0.01	0.01	0.01	0.01	0.02	0.01	0.01	0.01	0.01	0.01	0.01	0.01	0.01
Na	0.12	0.12	0.12	0.02	0.08	0.02	0.08	0.08	0.07	0.07	0.04	0.02	0.05	0.05	0.08	0.08	0.08	0.07	0.03	0.03	0.02	0.02
K	0.88	0.83	0.87	1.77	1.84	1.51	0.95	0.92	0.95	0.91	1.91	1.94	1.85	1.93	0.95	0.93	0.94	0.94	1.88	1.95	1.95	1.91
F	--	0.01	0.02	0.14	0.19	0.09	0.01	--	0.04	0.01	0.10	0.13	0.06	0.08	--	--	--	0.02	0.14	0.02	0.10	0.12
Cl	--	0.00	--	0.01	0.03	0.01	--	--	--	--	0.01	0.01	0.01	0.01	0.00	--	--	0.00	0.01	0.01	0.01	0.01
Tot	7.02	6.98	7.01	15.75	15.81	15.63	7.06	7.03	7.07	7.02	15.69	15.73	15.61	15.67	7.05	7.04	7.05	7.05	15.83	15.77	15.77	15.72

Atoms per formula unit are based on 11 oxygens for white mica and 22 for biotite. Abbreviation: Sp - micas on the main foliation; cor - coronitic micas around garnet; b.d. – below detection limit.
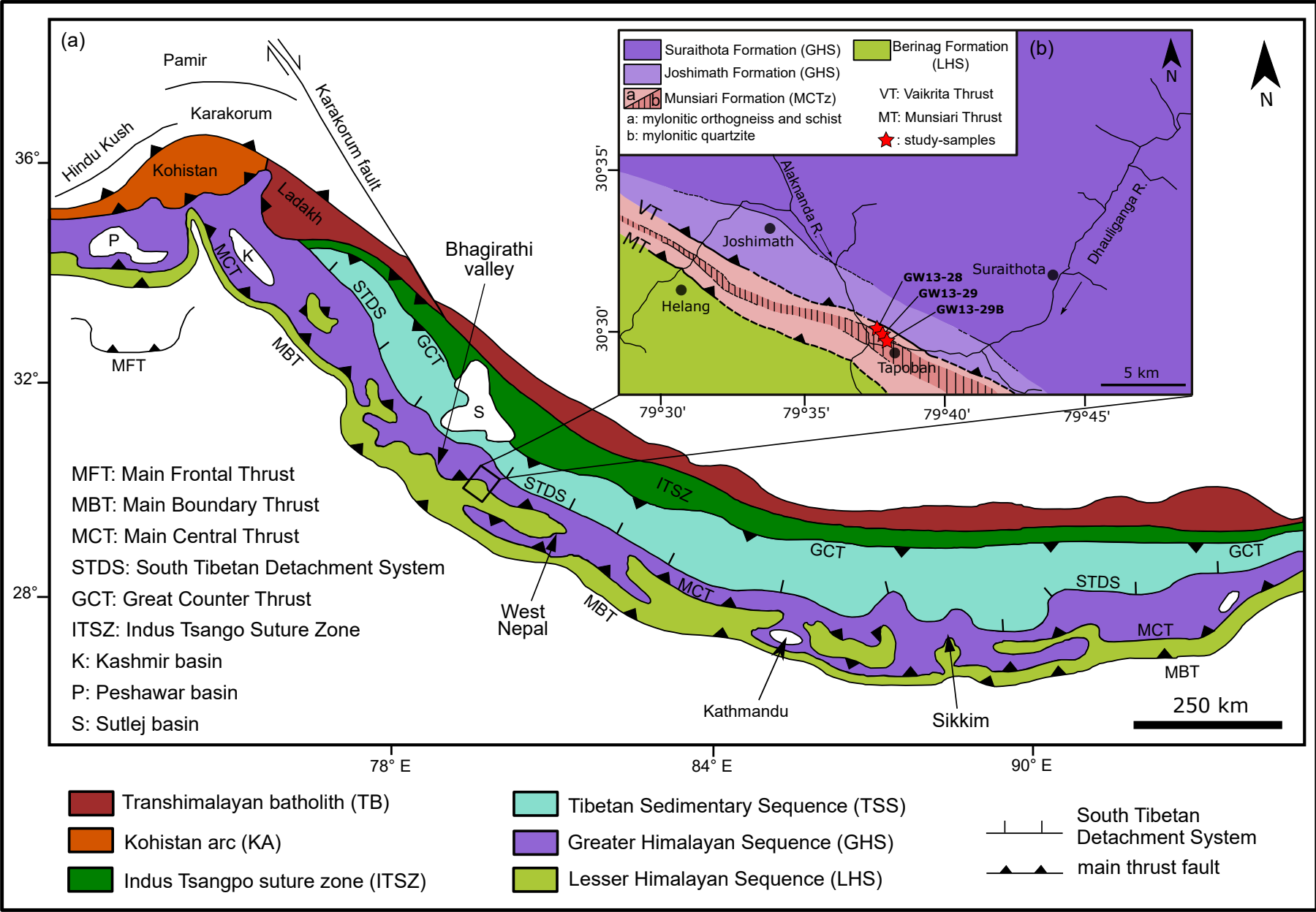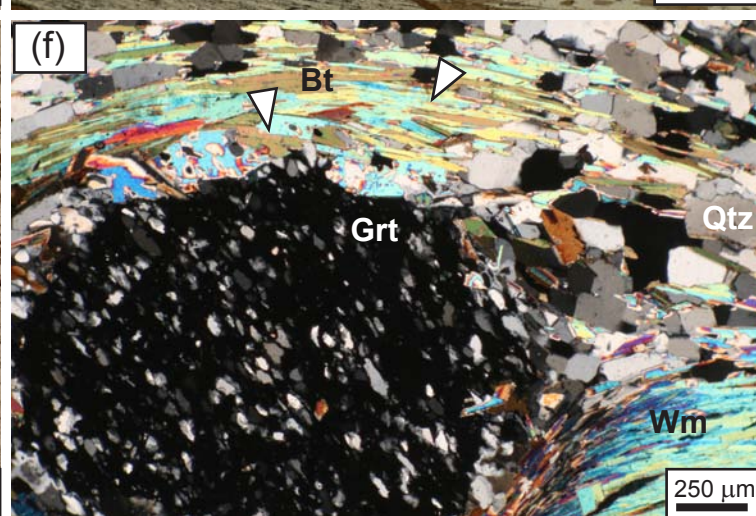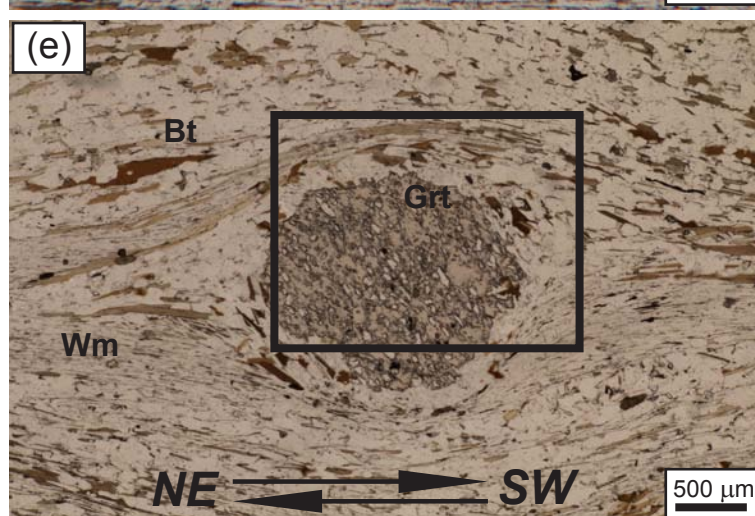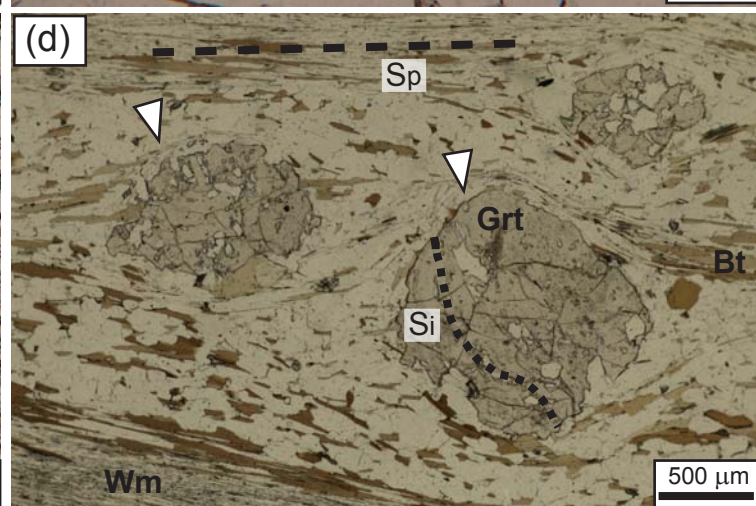
Figure 1

Figure 1

Figure 2

Figure 3

Figure 4

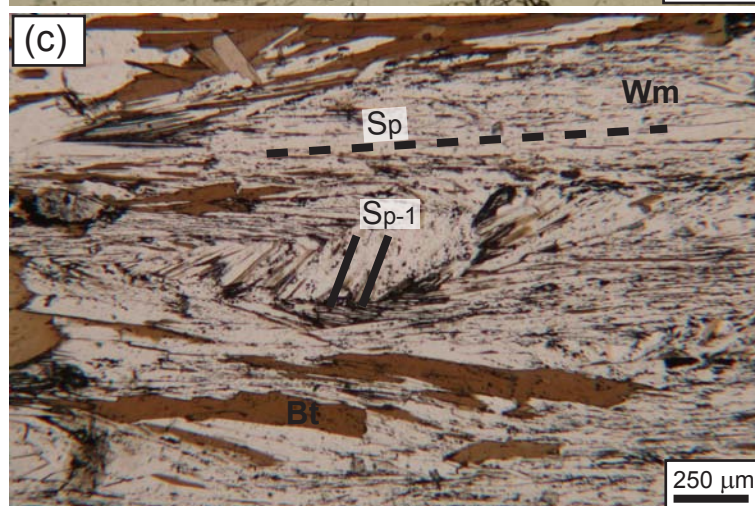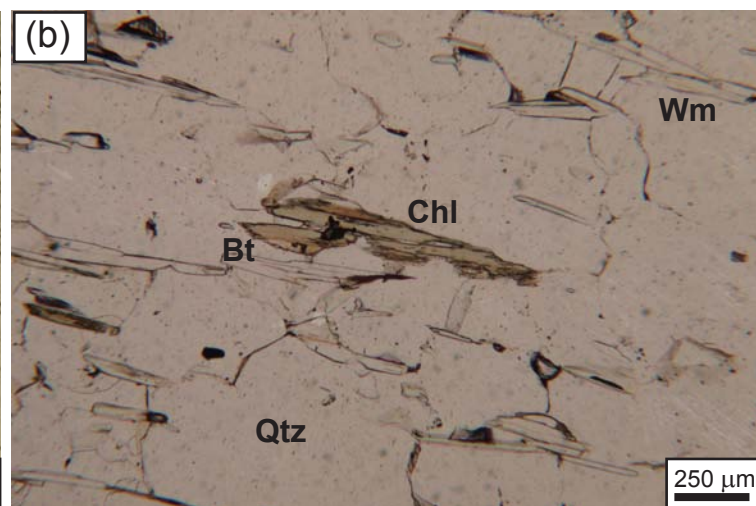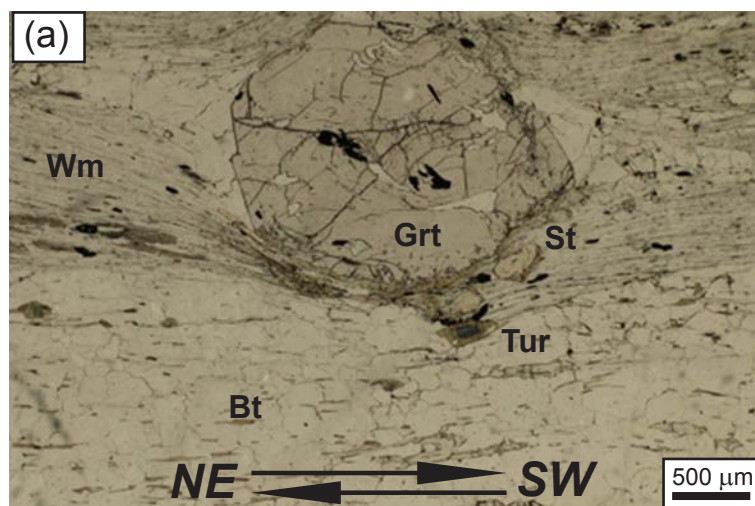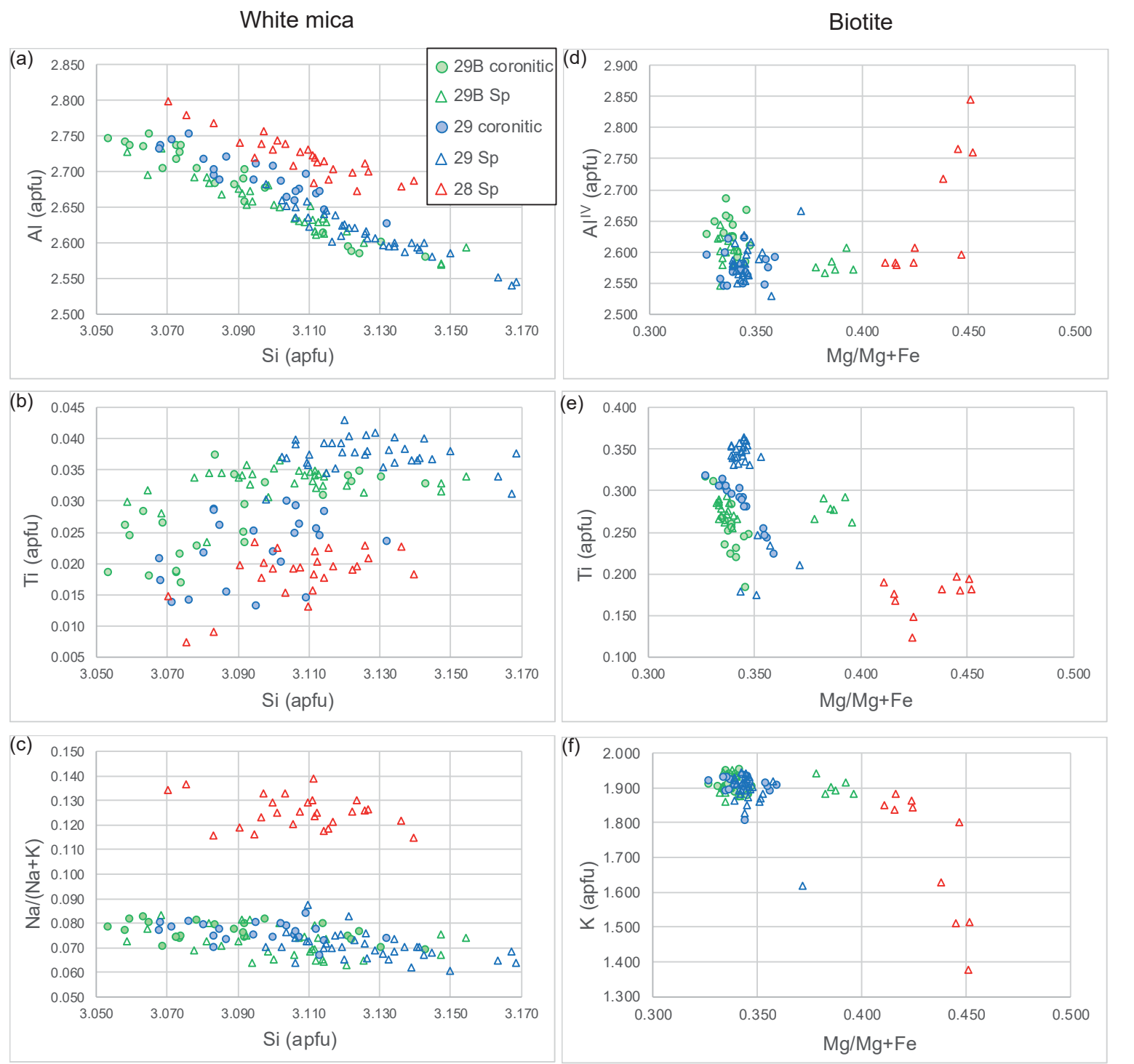Figure 5   Click here to download Figure Montemagni et al._Fig.5.pdf ⬇